

This item is the archived peer-reviewed author-version of:

Roles of distal aspartate and arginine of B-class dye-decolorizing peroxidase in heterolytic hydrogen peroxide cleavage

Reference:

Pfanzagl Vera, Nys Kevin, Bellei Marzia, Michlits Hanna, Mlynek Georg, Battistuzzi Gianantonio, Djinovic-Carugo Kristina, Van Doorslaer Sabine, Furtmueller Paul G., Hofbauer Stefan,- Roles of distal aspartate and arginine of B-class dye-decolorizing peroxidase in heterolytic hydrogen peroxide cleavage
Journal of biological chemistry - ISSN 0021-9258 - 293:38(2018), p. 14823-14838
Full text (Publisher's DOI): <https://doi.org/10.1074/JBC.RA118.004773>

Roles of distal aspartate and arginine of B-class dye-decolorizing peroxidase in heterolytic hydrogen peroxide cleavage

Vera Pfanzagl¹, Kevin Nys², Marzia Bellei³, Hanna Michlits¹, Georg Mlynek⁴, Gianantonio Battistuzzi⁵, Kristina Djinovic-Carugo⁴, Sabine Van Doorslaer², Paul G. Furtmüller¹, Stefan Hofbauer¹, and Christian Obinger^{1*}

From the ¹Department of Chemistry, Division of Biochemistry, BOKU - University of Natural Resources and Life Sciences, 1190 Vienna, Austria; ²Department of Physics, University of Antwerp, Antwerp, Belgium; ³Department of Life Sciences, University of Modena and Reggio Emilia, via Campi 103, 41125 Modena, Italy; ⁴Department for Structural and Computational Biology, Max F. Perutz Laboratories, University of Vienna, 1030 Vienna, Austria; ⁵Department of Chemistry and Geology, University of Modena and Reggio Emilia, 41125 Modena, Italy

Running title: *Mechanism of Compound I formation in KpDyP*

*To whom correspondence should be addressed: Christian Obinger: Department of Chemistry, Division of Biochemistry, BOKU - University of Natural Resources and Life Sciences, 1190 Vienna, Austria; christian.obinger@boku.ac.at; Tel. +43-1-47654-77273; Fax. +43-1-47654-77259.

Keywords: heme, enzyme kinetics, *Klebsiella pneumoniae*, pre-steady-state kinetics, site-directed mutagenesis, X-ray crystallography, electron paramagnetic resonance (EPR), heme peroxidase, oxoiron

ABSTRACT

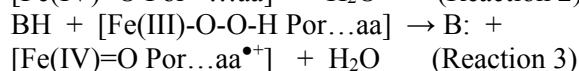
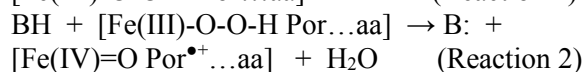
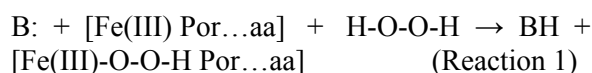
Dye-decolorizing peroxidases (DyPs) represent the most recently classified hydrogen peroxide dependent heme peroxidase family. Although widely distributed with more than 5000 annotated genes and hailed for their biotechnological potential detailed biochemical characterization of their reaction mechanism remains limited. Here, we present the high resolution crystal structures of wild-type B-class DyP from the pathogenic bacterium *Klebsiella pneumoniae* (*KpDyP*) (1.6 Å) and the variants D143A (1.3 Å), R232A (1.9 Å), and D143A/R232A (1.1 Å). We demonstrate the impact of elimination of the DyP-typical, distal residues Asp 143 and Arg 232 on (i) the spectral and redox properties, (ii) the kinetics of heterolytic cleavage of hydrogen peroxide, (iii) the formation of the low-spin (LS) cyanide complex as well as on (iv) the stability and reactivity of an oxoiron(IV)porphyrin π -cation radical (Compound I). Structural and functional studies reveal that the distal aspartate is responsible for deprotonation of H₂O₂ and for the poor oxidation capacity of Compound I. Elimination of the distal arginine promotes a collapse of the distal heme cavity including blocking of one access channel and a conformational change of the catalytic aspartate. We also provide evidence of formation of

an oxoiron(IV)-type Compound II in *KpDyP* with absorbance maxima at 418, 527 and 553 nm. In summary, a reaction mechanism of the peroxidase cycle of B-class DyPs is proposed. Our observations challenge the idea that peroxidase activity toward conventional aromatic substrates is related to the physiological roles of B-class DyPs.

Dye-decolorizing peroxidases (DyPs) are heme *b* containing oxidoreductases that catalyze the hydrogen-peroxide-mediated oxidation of various substrates. Their discovery and characterization (1,2) led to the classification as a novel heme peroxidase family with predominantly bacterial origin (3). These metalloenzymes have a distinct evolutionary origin, tertiary structure and active site architecture that significantly differ from members of other heme peroxidase superfamilies (4). Phylogenetic analysis shows three distinct phylogenetic classes, called A, B and C/D, which differ in structure, oligomeric state and predicted localization (5). Except for class C/D, where a role in lignin degradation is under discussion, the biological substrates are unknown. The enzyme investigated in this work originates from the human pathogen *Klebsiella pneumoniae* and belongs to class B.

Similar to classes A and C/D (1,2), all described B-class DyPs [*Rhodococcus jostii* (6,7), *Pseudomonas putida* (8), *Escherichia coli* (9), *Vibrio cholera* (10), *Enterobacter lignolyticus* (11)] exhibit peroxidase activities with conventional substrates [2,2-azinobis(3-ethylbenzothiazoline-6-sulfonic acid) (ABTS), guaiacol, pyrogallol, veratryl alcohol, hydroquinones etc.], antraquinone-derived dyes (e.g. Reactive Blue 19), Mn(II)-ions, or even lignin model compounds (6,10-13). However, compared to other heme peroxidase families the reported k_{cat}/K_m values are relatively small, thus raising the question about *in vivo* electron donors. Diverse enzymatic functions have been proposed for B-class DyPs, including deferrochelataase (9), porphyrin oxidase (14), or lignin peroxidase activity (12). However, in large parts direct biochemical and biophysical evidence of the suggested functions is missing.

In all heme peroxidase (super)families (4) the peroxidase cycle is initiated by deprotonation of hydrogen peroxide mediated by a distal base (B:) and formation of a short-lived ferric hydroperoxide [Fe(III)-O-O-H] complex, often designated as Compound 0 (Reaction 1). Heterolytic cleavage of the O-O bond mediates the two-electron oxidation of Compound 0 to Compound I, thereby forming an oxoiron(IV) species [Fe(IV)=O] in combination with either a porphyrin radical (Por^{•+}) (Reaction 2) or a distinct amino acid radical (aa^{•+}) (Reaction 3). Additionally, water is released.



In two heme peroxidase superfamilies (peroxidase-catalase and peroxidase-cyclooxygenase superfamilies) (4) Compound I formation is described to involve acid-base catalysis through the highly conserved His-Arg couple in the distal side, known as the Poulos-Kraut mechanism (15,16). In all DyP classes an Asp-Arg couple is found at the distal side (4). However, the distinct functional role of the distal catalytic amino acids in the heterolytic cleavage of H₂O₂ is still under dispute. In B-class DyPs both the Arg [DyPs from *R. jostii* RHA1 (7) and *P. putida* (8)] and the Asp [DyP

from *E. lignolyticus*, *EIDyP* (11)] have been proposed to act as proton acceptor and donor in Compound I formation. In A- and C/D-classes the distal Asp was suggested to act as acid-base catalyst (3,17). Likewise, the mechanism of Compound I reduction and the electronic features of Compound II of B-class DyPs remain elusive. Based on studies of solvent isotope and viscosity effects on Compound I reduction of *EIDyP* it was proposed that the reducing substrate binds to Compound I instead of free enzyme and mediates its two-electron reduction without formation of an oxoiron(IV)-type Compound II (11).

Here we hypothesize that the distal aspartate acts as proton acceptor during heterolytic cleavage of hydrogen peroxide. This hypothesis is based on the facts that (i) B-class DyPs typically exhibit pH optima of enzymatic activity below pH 7 and deprotonation of a guanidinium group (pK_a = 13.8) (18) *per se* below pH 10 is thermodynamically unfavourable even in a hydrophobic micro-environment (18), and that (ii) the distal Arg in B-class DyPs forms a salt bridge with propionate p7 of the prosthetic group, which favours the protonated state of the guanidinium group to a greater extent. In order to confirm this hypothesis we elucidate the crystal structures of wild-type *KpDyP*, the single variants D143A and R232A as well as the double variant D143A/R232A, and perform a comprehensive biochemical and biophysical characterization of those proteins. Our study confirms the essential function of D143 in hydrogen peroxide reduction and of Arg232 in maintenance of the distal architecture. Compound I of B-class DyPs is shown to be an oxoiron(IV)porphyrin π -cation radical of very poor oxidation capacity, whereas substitution of D143 significantly increases the two- and one- electron oxidation capacity of Compound I. Furthermore, we demonstrate the formation of an oxoiron(IV)-type Compound II for both wild-type *KpDyP* and the variant D143A.

Results

Recombinant *KpDyP* is a stable homodimeric high-spin ferric heme protein

As a basis for elucidation of the role of D143 and R232 in heterolytic cleavage of H₂O₂ we aimed at characterization of the solution and crystal structures of wild-type *KpDyP* and its variants D143A, R232A and D143A/R232A. Consequently these proteins were expressed heterologously in

E. coli and purified by affinity and size-exclusion (SEC) chromatography as described in experimental procedures. Typically, 60-80 mg wild-type and variant heme protein per liter culture broth were obtained. HPLC-SEC combined with multi-angle light scattering confirmed the presence of pure homodimeric wild-type and variant proteins (2×35 kDa) (data not shown), which is in accordance with previously published B-class DyPs. The average Reinheitszahl (RZ, A_{Soret}/A_{280}) was found to be 2.1 (wild-type *KpDyP*), 1.7 (D143A) and 2.7 (R232A and D143A/R232A), respectively. Upon using the pyridine-hemochromogen assay (19), the extinction coefficients at the Soret maxima were determined to be $160\,000\text{ M}^{-1}\text{ cm}^{-1}$ (wild-type *KpDyP*, D143A) and $240\,000\text{ M}^{-1}\text{ cm}^{-1}$ (R232A, D143A/R232A), respectively.

Figures 1A and 1B depict the UV-Vis and EPR spectral signatures of wild-type *KpDyP* and the variants. At pH 7.0 all proteins are in the high-spin (HS) state. Wild-type *KpDyP* exhibits UV-vis bands at 405 nm (Soret band) together with a small shoulder at 385 nm, 507 nm and 539 nm (Q-bands) and 640 nm [charge transfer (CT) band]. Except for the broad Soret maximum at 400 nm the spectrum of the D143A variant is identical with that of the wild-type protein. In the variants R232A and D143A/R232A the CT band is blue-shifted to 630 nm, whereas the other bands are almost wild-type-like (R232A: 405, 505, 539 nm; double variant: 405, 503, 539 nm). Except for the D143A variant no spectral changes were observed between pH 4.5 and pH 10. In case of D143A an alkaline transition occurred ($\text{p}K_{\text{a}} = 8.6$) resulting in a species with Soret maximum at 410 nm and additional bands at 540, 576 and 610 nm, indicative of the presence of a HS hydroxo ligand (Fig. 1A and Supplemental Fig. S1) or a mixed population of HS and LS hydroxo ligated heme iron.

The effect of the catalytic amino acids on the heme surrounding and electronic state of the heme iron of *KpDyP* was further investigated using low-temperature CW EPR spectroscopy. The experimental spectra of ferric wild-type *KpDyP* and its distal side variants at neutral pH (Fig. 1B) clearly display the presence of high-spin (HS, $S = 5/2$) Fe(III) heme centres, which was not influenced by pH (data not shown). Due to the large zero-field splitting, the X-band EPR spectra can be simulated in two ways (20). On the one hand, they can be described as a $S=5/2$ system with g values close to 2

and varying E/D values (with D and E being the tetragonal and rhombic zero-field splitting, respectively). On the other hand, the EPR spectra can also be simulated assuming an apparent $S=1/2$ system with effective g^{eff} tensor. Both approaches were assumed here, in order to allow comparison with literature data (Table 1). For each *KpDyP* variant, the presence of multiple HS species with varying rhombicity was found as reflected by the different E/D -values. Table 1 and Figure 1B reveal that site-directed mutation of the catalytic amino acids Arg232 and Asp143 in *KpDyP* strongly influences the EPR spectra, implying a marked change of the heme pocket sensed by the heme iron. Even though the heme-pocket heterogeneity remains, the dominant contribution appears to be much less rhombic.

Exclusively in the case of ferric wild-type *KpDyP*, an organic radical is also observed (Fig. 1B). The features and g -anisotropy (g values in the 2.002-2.009 range) of this EPR signal (see top inset of Fig. 5) suggest the presence of one or more tyrosyl radicals (21,22). Although amino-acid radicals have been observed in DyPs after activation of the enzyme with H_2O_2 , they have, to our knowledge, never been reported for the resting state of the enzyme (22-25).

The electronic circular dichroism (ECD) spectra in the far-UV (190-250 nm, data not shown) and near-UV region (250-350 nm) of the four proteins were almost identical suggesting that the mutations did not change the overall secondary and tertiary structure. By contrast, ECD spectra in the visible region showed differences, again reflecting altered heme cavity architectures in the four proteins. At pH 7.0 wild-type *KpDyP* shows a Soret minimum at 411 nm, whereas in the variant D143A the minimum is broadened and shifted to 407 nm. Additionally, both wild-type *KpDyP* and D143A exhibit a small peak around 373 nm. In case of the variants R232A and D143A/R232A the ellipticity at the sharpened minimum at 411 nm is increased (Fig. 1C).

Next, we probed the standard reduction potential (E°) of the Fe(III)/Fe(II) redox couple of *KpDyP* and its catalytic variants by spectroelectrochemical titration at pH 7.0. Upon reduction of ferric to ferrous wild-type *KpDyP* the Soret peak shifts from 405 nm to 435 nm. Figure 2 shows the fully oxidized and fully reduced (black and red lines, respectively) as well as the equilibrium spectra of wt *KpDyP* (grey lines) at seven different

applied potentials in the optical transparent thin-layer spectroelectrochemical (OTTLE) cell (25 °C, pH 7.0). The calculated reduction potential E° for the Fe(III)/Fe(II) couple, determined from the corresponding Nernst plot (inset to Fig. 2), was calculated to be -0.350 ± 0.010 V. Removal of D143 slightly increases the standard reduction potential (D143A: -0.330 ± 0.010 V) compared to the wild-type protein, whereas E° is almost unaffected by elimination of R232 (R232A: -0.347 ± 0.010 V). The E° value of D143A/R232A was calculated to be -0.299 ± 0.010 V.

Finally, we probed the thermal stability of wild-type *KpDyP* between pH 3 and pH 8 by differential scanning calorimetry (DSC) since DyPs are often described for optimum peroxidase activity at acidic pH (< pH 3.0). As is appropriate for a cytoplasmatic protein, wild-type *KpDyP* was found to be most stable between pH 5.5 and pH 7.0 (Fig. 1D). Temperature-mediated unfolding shows one endotherm that can be best fitted by assumption of a non-two-state transition with two consecutive irreversible unfolding events at T_m values of ~ 58 °C and ~ 60 °C at pH 5.5, which cannot be separated. This All variants exhibited decreased thermal stability but followed a similar unfolding profile and pH dependence. Typically, the T_m values of the mutants were lowered by 5-10 °C following the hierarchy wild-type > D143A > R232A > D143A/R232A. Please note that below pH 4 wild-type *KpDyP* was too unstable and aggregated upon heating.

Distal D143 is essential for pH-independent Compound I formation

Before investigating Compound I formation of *KpDyP*, we probed the kinetics and thermodynamics of the formation of the cyanide complex of *KpDyP* and the three variants, since cyanide binding mechanistically mirrors Compound I formation. Cyanide, which at most biological pHs is protonated ($pK_a = 9.14$), binds as an anion to Fe(III). Thus, HCN and H_2O_2 need to be deprotonated by a distal base. Thereby deprotonation of HCN mimics the committing step of H_2O_2 -mediated Compound I formation. Upon addition of cyanide high-spin wild-type and *KpDyP* variants are converted to a low-spin complex with a Soret maximum at 420 nm. Spectrophotometric titration of *KpDyP* revealed that the dissociation constant (K_D) of the wild-type protein is very high (900 ± 40 μ M).

Elimination of R232 increased K_D (2700 ± 370 μ M). In the double variant K_D was determined to be 136 ± 13 μ M (data not shown). By contrast, binding affinity of cyanide was significantly increased upon elimination of the distal aspartate (D143A: 20 ± 12 μ M derived from pre-steady state kinetics).

Next we probed the kinetics of cyanide binding by stopped-flow spectroscopy. At pH 7.0 the apparent second order rate constant, k_{on} , of the reaction between wild-type *KpDyP* and cyanide was determined to be $(7.6 \pm 0.2) \times 10^4$ $M^{-1} s^{-1}$ (Fig. 3). Between pH 4.0 and pH 9.0 the k_{on} values remained almost unchanged (ca. 40% increase between pH 5.0 and 8.0). By contrast, cyanide binding to D143A strongly depended on pH, ranging from $(5.9 \pm 0.6) \times 10^2$ $M^{-1} s^{-1}$ at pH 5.0 to $(2.3 \pm 0.2) \times 10^5$ $M^{-1} s^{-1}$ at pH 8. At pH 7, k_{on} of D143A was almost wild-type-like ($4.6 \pm 0.6) \times 10^4$ $M^{-1} s^{-1}$). Upon elimination of R232 cyanide binding was drastically reduced [$(13 \pm 1) M^{-1} s^{-1}$, pH 7.0], whereas k_{on} for the double variant was calculated to be $(6.1 \pm 0.4) \times 10^3$ $M^{-1} s^{-1}$ at pH 7.0 (Fig. 3).

Next we focused on the role of D143 and R232 in Compound I formation. Oxidation of wild-type *KpDyP* to Compound I mediated by hydrogen peroxide was followed in the conventional stopped-flow mode (Fig. 4A). Compound I is characterized by a Soret maximum at 397 nm ($\sim 50\%$ hypochromicity compared to ferric *KpDyP*) and formation of an additional band at 648 nm. The reaction is monophasic ($k_{app} = (6.2 \pm 0.2) \times 10^6$ $M^{-1} s^{-1}$ at pH 7.0) with clear isosbestic points at 430 and 550 nm (Fig. 4A). Compound I is already formed with equimolar H_2O_2 and its UV-vis spectrum remains unchanged for minutes, whereas at high excess of H_2O_2 (> 1 mM) heme is degraded within seconds as reflected by loss of absorbance and generation of a peak at 670 nm which might indicate biliverdin formation (26). Similar to cyanide binding, Compound I formation of wild-type *KpDyP* is pH independent between pH 4 and pH 9 (not shown).

Upon addition of hydrogen peroxide to the variants similar spectral transitions were observed (Fig. 4B-4D). However, a ~ 400 -fold stoichiometric excess of H_2O_2 is necessary in order to obtain full hypochromicity at the Soret band and the apparent bimolecular rate constants are diminished by 3 orders of magnitude (insets to Fig. 4C and 4D). Moreover, the variants R232A ($k_{app} = (2.2 \pm 0.1) \times 10^3$ $M^{-1} s^{-1}$ at pH 7.0) and D143A/R232A ($k_{app} = (4.5$

$\pm 0.2 \times 10^3 \text{ M}^{-1} \text{ s}^{-1}$ at pH 7.0) are significantly more prone to heme degradation compared to the wild-type protein. Heme degradation is reflected by the biphasic kinetics of Compound I formation with the second slow phase representing bleaching of the prosthetic group. In case of D143A Compound I formation ($k_{\text{app}} = 1.9 \pm 0.1 \times 10^3 \text{ M}^{-1} \text{ s}^{-1}$ at pH 7.0) (inset to Fig. 4B) is followed by a slow H_2O_2 -dependent conversion ($k_{\text{app}} = 40 \text{ M}^{-1} \text{ s}^{-1}$) to a species reminiscent of classical oxoiron(IV)-type Compound II with absorbance maxima at 417, 527 and 555 nm (red spectrum in Fig. 4B). Similar to cyanide binding, the k_{app} values of Compound I formation of the variant D143A increase between pH 5.0 ($1.4 \pm 0.1 \times 10^2 \text{ M}^{-1} \text{ s}^{-1}$) and pH 8.0 ($8.6 \pm 0.1 \times 10^3 \text{ M}^{-1} \text{ s}^{-1}$). By contrast, Compound I formation of R232A slightly increases with decreasing pH.

Compound I is an oxoiron(IV) porphyrin π -cation radical

Next we probed the electronic configuration of Compound I by EPR spectroscopy at 2.5 K. Compound I was formed by addition of a 5-fold molar excess of H_2O_2 to wild-type KpDyP (Fig. 5, lower panel). The corresponding CW EPR spectrum exhibits radical-type signals and some residual HS Fe(III). Closer inspection of the former (Fig. 5, inset to lower panel) reveals that this signal is composite, displaying two features with a different saturation behavior (Fig. S2A in SI). The most intense peak at $g = 2.00$ is in good agreement with the porphyrin π -cation radical observed in horseradish peroxidase (Fig. S2C) (27,28). This intense signal disappears upon increase of the temperature above 10 K leaving only the lower intense radical signal of the composite EPR part (Fig. S2B). A similar behavior is observed after H_2O_2 -activation of DyP from *Thermomonospora curvata* (23). Multi-frequency pulsed EPR experiments in combination with site-directed mutagenesis are currently on-going to further elucidate the nature of all species in the resting and activated states.

KpDyP forms a classical oxoiron(IV)-type Compound II

Next we probed the enzymatic activity of KpDyP and investigated the spectral features of the involved redox intermediates of this heme peroxidase. Wild-type KpDyP exhibits very poor overall peroxidase activities. Oxidation of bulky dyes like RB19, reactive black 5, indigo carmine and acid red 183

was extremely slow. This also applies to conventional peroxidase substrates like guaiacol, pyrogallol, 3,3',5,5'-Tetramethylbenzidine (TMB), catechol, hydroquinones, tyrosine and ascorbate (< 0.5 units/mg) (not shown). Only ABTS was an exception, but also its oxidation is modest (~ 40 units/mg). Looking for alternative enzymatic activities (e.g. hydroxylation, dehalogenation, N-oxidation etc.) was without results.

Finally, we have probed the direct reaction between preformed Compound I of wild-type KpDyP and the D143A variant with various putative one- and two-electron donors in the multimixing stopped-flow mode (Fig. 6). Regarding two-electron donors, chloride and bromide did not react with wild-type KpDyP Compound I (formed with 2-fold stoichiometric excess of H_2O_2), whereas iodide reacted only to a limited extent. Thiocyanate mediates the slow conversion of wild-type Compound I directly to the ferric state with isosbestic points at 356, 452 and 553 nm (Fig. 6A). The time traces monitored at 386 nm (isosbestic point between Compound I and Compound II, see below), 405 nm (Soret maximum of ferric state) and 420 nm (isosbestic point between Compound II and ferric state) are biphasic and show an initial lag phase followed by slow formation of the ferric state mediated by 1 mM thiocyanate. The lag phase may reflect cycling due to excess of H_2O_2 as its length increases with increasing excess of H_2O_2 . No lag phase is observed when substoichiometric concentrations of H_2O_2 are used.

Elimination of D143 significantly increased Compound I reactivity towards thiocyanate. (Fig. 6B). Compound I was formed with a 500-fold stoichiometric excess of H_2O_2 . Upon reaction with thiocyanate ferric D143A was formed rapidly and directly with clear isosbestic points at 432, 455 and 538 nm. Figure 6B shows a representative time trace of the reaction between D143A Compound I and 10 μM thiocyanate. Due to the excess of H_2O_2 necessary for Compound I formation, exact determination of the apparent second-order rate constant was not possible ($> 10^6 \text{ M}^{-1} \text{ s}^{-1}$).

Next we probed Compound I reduction by serotonin. It has to be noted that addition of TMB leads to comparable spectral changes as described for serotonin while ascorbate and hydroquinone mediate only slow spectral conversions ($k_{\text{obs}} > 0.5 \text{ s}^{-1}$ with 1 mM). Tyrosine did not react at all (Fig. S3). Figure 6C shows the reaction between wild-type

KpDyP Compound I (green spectrum) and 50 μM serotonin at pH 7.0. Compared to the direct two-electron reduction of Compound I to ferric *KpDyP*, different spectral transitions were observed. During the very slow reaction a redox intermediate accumulated after 15-20 s with spectral features reminiscent of oxoiron(IV)-type Compound II (absorbance bands at 527 nm and 556 nm; red spectrum in Fig. 6C). Finally, this intermediate slowly disappeared and the spectrum of ferric wild-type *KpDyP* was formed (black spectrum). This conversion (Compound I \rightarrow Compound II \rightarrow ferric state) is also reflected by biphasic time traces monitored at 405 and 420 nm but not 386 nm (i.e. isosbestic point between Compound I and Compound II).

Again, the reactivity of the D143A variant Compound I with serotonin was several orders of magnitude higher at pH 7.0 compared to the wild-type enzyme (Fig. 6D). Conversion of D143A Compound I to an oxoiron(IV)-type Compound II (418, 527 and 553 nm, red spectrum in Fig. 6D) was monophasic with clear isosbestic points at 397, 450, 502 and 572 nm. No further transitions were observed probably due to excess of H_2O_2 and cycling of the variant. The apparent second-order rate constant k_{app} of Compound I reduction by serotonin was estimated to be $\sim 10^4 \text{ M}^{-1} \text{ s}^{-1}$.

Finally, we have analysed the serotonin-mediated reaction of Compound I by the ProK global analysis software (Applied Photophysics). Spectral simulation allowed isolation of the spectral features of ferric state, Compound I and Compound II of wild-type *KpDyP* at pH 7.0 and pH 10.0 during time course of reaction (Fig. S3). Data clearly support the step-wise formation of Compound I and oxoiron(IV)-type Compound II. However, in the wild-type enzyme (in contrast to the D143A variant) Compound II never fully accumulated. At pH 7.0 always a mixture of dominating Compound I, Compound II (<20%) and ferric state (<10%) is present. This ratio differs at pH 10 (50% Compound I, 40% Compound II, 10% ferric state) (Fig. S3C & S3D). In any case, these findings clearly demonstrate that dye-decolorizing peroxidases of class B follow the classical peroxidase cycle with an oxoiron(IV)-type Compound II as redox intermediate.

Heme active site conformation is compromised by substitution of R232

Finally, we elucidated the crystal structures of *KpDyP* and the three variants at high resolution. The wild-type structure was solved by molecular replacement using the DyP structure from *Vibrio cholera* (*VcDyP*). For the variants the wild-type structure was used as a replacement model. The structures were refined to a resolution of 1.6 Å (wild-type), 1.27 Å (D143A), 1.86 Å (R232A) and 1.09 Å (D143A/R232A). Data collection and refinement statistics are given in Table 2, a comparison of the $2F_o - F_c$ electron density maps contoured at $\sigma = 1.5$ of the active site is shown in Figure S5.

All structures exhibit a dimeric ferredoxin-like fold typical for dye-decolorizing peroxidases, composed of antiparallel β -sheets with four β -strands connected by α -helices. Figure 7 depicts the structure of wild-type *KpDyP*. For all figures we use the chain A subunit, but both subunits are in good agreement with respect to amino acid position, ligands and intramolecular distances if not noted otherwise. One heme *b* cofactor is present per subunit with H215 acting as proximal ligand at a distance of 2.2 Å between the heme iron and N ϵ . The proximal ligand is hydrogen bonded to D268.

At the distal heme side a pronounced hydrogen bonding network is observed, including the proposed catalytic residues D143 and R232, water molecules (W1, W5, W4, W3) and propionate p6. Propionate p6 and p7 are connected by hydrogen bonding via the water molecule W2. Importantly, a salt bridge between R232 and propionate p7 stabilizes the distal architecture. As already observed in other B-class DyP structures, there are two access channels to the heme. The distal access channel to the active site pocket comprised of D143, R232, F248, L246 and S234 is narrow with a calculated bottle neck radius of 1.2 Å (calculated by CAVER). The second access from the surface is via the solvent exposed propionate p6 (Fig. 7).

Substitution of the distal residues D143 and R232 did not lead to significant changes in the overall fold of the enzyme. Exchange of D143 by alanine does not change the active site architecture (Fig. 8 and S5). However, in D143A the distal access channel is significantly bigger, while the surface exposure of propionate p6 remains similar to the wild-type protein (Fig. 8). In the structures of D143A a molecule of unknown origin (refined as nitrite) was repeatedly found ligated to the heme iron at a distance of 2 Å. However, the presence of this ligand

had no impact on the conformation of the distal residues.

In contrast to D143A, the R232A variant shows significant changes in the active site conformation, with residues 142-148 found in a completely different orientation compared to the wild-type structure (Fig. S4). These structural alterations might cause the different space group of the crystal structure of R232A compared to wt *KpDyP* despite very similar crystallization conditions (Table 2). The residues 142-148 form a loop which amounts to 50% of the solvent exposed active site. The new loop conformation in R232A is stabilized on one side through two hydrogen bonds formed between D143 and the nearby R131 and one between T135 and R232 as well as on the other side by the change of P148 from a trans- to a cis-conformation. In the crystal structure of R232A, D143 is pointing away from the heme *b* cofactor and the distance between the carboxylate oxygen and the heme iron increases from 5.0 Å to 8.9 Å. In addition, reorientation of the loop leads to the loss of the distal access channel, while both heme *b* propionates are completely solvent-exposed. Notably, the orientation of the propionate p7 also changes, most likely due to the missing salt bridge. The closest distal water is 4.96 Å away from the heme iron in chain A and 4.1 Å in chain B.

Interestingly, the crystal structure of the variant D143A/R232A is similar to the wild-type structure. Simultaneous substitution of D143 and R232 by alanine leads to increased accessibility of the active site through the distal access channel. It is noteworthy that crystals could only be obtained with the addition of 5% glycerol. As a consequence, a glycerol molecule occupies the position of substituted R232 in D143A/R232A and is extensively involved in hydrogen bonding with the propionate p7 and surrounding water molecules. We propose that this glycerol replaces R232 in its role to stabilize the wild-type-like conformation of the loop comprising residues 142-148. In the double variant, the distal iron coordination position is occupied by a water molecule at a distance of 2.2 Å.

Discussion

In the present study we have aimed to elucidate the mechanism of Compound I formation and reduction by comparison of wild-type *KpDyP* and variants having the conserved putative catalytic distal residues D143 and R232 exchanged by

alanine. Importantly, the recombinantly produced variants D143A, R232A and D143A/R232A showed wild-type-like ECD-spectra in the far- and near-UV region and similar, albeit slightly lower, pH-dependent thermal stabilities as the wild-type protein. Moreover, the high resolution crystal structures of wild-type *KpDyP* and the investigated variants showed that the performed mutations did not alter the overall fold which is similar to other B-class DyPs (6, 10-11). Together these findings demonstrated that between pH 4.5 and pH 9.0 all four proteins were correctly folded and thus allowed comparative kinetic studies within this pH regime.

In all DyPs the prosthetic group, i.e. heme *b*, is coordinated by a proximal histidine (H215) which is hydrogen bonded with a fully conserved aspartate (D268). The negative standard reduction potential E° of the Fe(III)/Fe(II) couple of -350 mV clearly suggests a pronounced imidazolate character of H215 in *KpDyP*. In other B-class DyPs the corresponding E° values were reported to be more positive, e.g. -260 mV in *PpDyP* (8) and -290 mV in *EdDyP* (11). Interestingly, the impact of the introduced substitutions is relatively small. Elimination of a negative charge by exchange of D143 by alanine should increase E° [Fe(III)/Fe(II)]. However, in D143A the small effect (+20 mV) seems to reflect the increase in exposure of the heme iron to solvent compared to wt *KpDyP* (Fig. 8). By contrast, elimination of a positive charge in the heme cavity should decrease the reduction potential. Here, substitution of R232 by alanine does not significantly influence the E° (-3 mV) which indicates that the loss of R232 is compensated by loss of the negatively charged carboxylate group of D143 that points away from the heme iron in R232A (Fig. 8). In any case, the ferric state is highly stabilized both in wild-type *KpDyP* and the variants.

We have demonstrated that the distal H-bonding network including D143, R232 and several water molecules (W1-W5) as well as the propionate side chains p6 and p7 of wild-type *KpDyP* is stable between pH 4.5 and pH 10.0, as is reflected by almost identical high-spin (HS) spectra determined by both UV-vis and EPR spectroscopy. No alkaline transition was observed suggesting identical distances between D143, R232, W1 and the heme iron in this pH regime. The variant D143A is unique in showing an alkaline transition ($pK_a = 8.6$) to a HS hydroxo state. For each *KpDyP* variant, EPR revealed the presence of multiple HS species with

varying rhombicity as reflected by the different E/D -values (Fig. 1B). Co-existence of several HS species is not uncommon for peroxidases (Table 1). Different HS forms were detected for catalase-peroxidase (KatG) from *M. tuberculosis* and these forms appeared to be pH dependent (29). The EPR spectra of chlorite dismutase from *Magnetospirillum* sp. showed different HS and LS features that were influenced by the purification method (30), NaCl excess (30), pH and ageing (31). On the contrary, only one HS species was found in the dimeric chlorite dismutase from *Cyanothece* sp. PCC7425 (CCld) (32). CW-EPR studies on the A-class DyP of *T. curvata* and a fungal DyP of *A. auricula-judae* also show a pH dependence of the HS forms and a heme-pocket heterogeneity, respectively (23,33). These proteins display, however, a much lower rhombicity of the dominant species than wild-type *KpDyP* (Table 1) and the A-class DyP from *R. jostii* RHA1 (34).

The crystal structures of wt *KpDyP* revealed two heme access channels. One narrow channel leads perpendicularly to the distal heme pocket and its small bottleneck radius of 1.2 Å suggests that it only allows access of H₂O₂ or small ligands like cyanide. This channel also exists in B-class DyPs of *R. jostii* RHA1, *VcDyP* and *ElDyP* with reported bottleneck radii of 2-3 Å. The second access channel is relatively open and leads to the solvent-exposed propionate p6. Here, principally, potential substrates could bind and deliver electrons. Exchange of D143 by alanine kept the heme cavity architecture wild-type-like, but significantly increased the distal channel diameter, whereas substitution of R232 by alanine induced a collapse and reorganization of the heme cavity leading to loss of the distal heme access channel. Additionally, in the crystal structure of R232A the side chain of D143 points away from the heme iron. These data indicate that it is not reliable to discuss the role of R232 in catalysis of Compound I formation in *KpDyP* based on the kinetic data of R232A. It remains open whether less drastic substitutions of R232 do not result in collapse of the heme pocket of *KpDyP*.

Oxidation of ferric wild-type *KpDyP* by hydrogen peroxide is extremely fast ($\sim 6.2 \times 10^6 \text{ M}^{-1} \text{ s}^{-1}$), monophasic and pH independent between pH 4 and pH 9. CW-EPR spectroscopic data recorded at 2.5 K revealed the electronic structure of Compound I to be an oxoiron(IV) porphyrin radical species. This is also reflected by the monitored UV-vis

spectral changes (i.e. 50% hypochromicity in the Soret region) during the reaction between ferric *KpDyP* and equimolar H₂O₂.

Compound I formation in heme peroxidases needs an initial interaction (“ligand binding”) of H₂O₂ with the ferric heme iron (reaction 1, k_1) (35). This is followed by deprotonation of H₂O₂ and binding of the resulting anion to the ferric heme iron (i.e. formation of so-called Compound 0) (reaction 2, k_2). Compound 0 formation is followed by rapid heterolytic cleavage of the peroxide bond (k_3), thereby forming Compound I and water (Reaction 3). In two heme peroxidase superfamilies (4), i.e. peroxidase-catalase and peroxidase-cyclooxygenase superfamilies, a fully conserved distal His-Arg pair supports Compound I formation. The distal His acts as acid-base catalyst and deprotonates the incoming H₂O₂ and protonates the distal oxygen during heterolytic cleavage. Additionally, the negatively charged outer oxygen atom seems to be transiently stabilized by the guanidinium group of the conserved arginine (15). The rates of Compound I formation in these peroxidases are similar ($1\text{-}5 \times 10^7 \text{ M}^{-1} \text{ s}^{-1}$) (36) and slightly higher compared to B-class DyPs. Typically in these peroxidases heterolytic cleavage of the O-O bond in Compound 0 is significantly faster than Compound 0 formation ($k_3 \gg k_2$). As a consequence Compound 0 is difficult to trap.

Our data support a similar mechanism for Compound I formation in B-class DyPs (Fig. 9) with distal D143 acting as acid-base catalyst. The observed pH-independence of Compound I formation within the range pH 4.0 to 9.0 indicate that the pK_a of the side chain of D143 is far below 4.0 since its conjugated base is stabilized through the proximity to the guanidinium group of R232. In the absence of D143 the apparent bimolecular rate constant of Compound I formation is reduced by three orders of magnitude at pH 7.0 and the pH independence disappears. Interestingly, while a similar impact was observed in *E. lignolyticus* (11) ($\sim 2 \times 10^2 \text{ M}^{-1} \text{ s}^{-1}$), the same substitution had only a minor impact on Compound I formation in *R. jostii* (7) ($9.4 \times 10^4 \text{ M}^{-1} \text{ s}^{-1}$ compared to $2 \times 10^5 \text{ M}^{-1} \text{ s}^{-1}$ in the wild-type protein). However, in A- and C/D-class DyPs it was demonstrated that the conserved distal aspartate is essential in Compound I formation (3, 18).

In the *KpDyP* variant D143A the rate of Compound I formation increases with increasing pH suggesting the assistance of hydroxide ions in H₂O₂

deprotonation. This scenario is also supported by the kinetics of cyanide binding to ferric wild-type *KpDyP* and to the variant D143A. Cyanide, which at most biological pHs is protonated ($pK_a = 9.14$), must also be deprotonated before binding to ferric heme proteins. Thus cyanide complex formation mirrors H_2O_2 -mediated formation of Compound 0 in peroxidases. Typically, the apparent bimolecular rate constant of cyanide complex formation of wild-type *KpDyP* is pH independent, whereas cyanide binding to D143A increases by one order of magnitude per pH step between pH 5.0 and pH 9.0. Consequently, our data suggest that Compound 0 formation (but not heterolytic cleavage of the O-O bond in Compound 0) is the rate limiting step in B-class DyPs. This was also proposed for Compound I formation in *EdDyP* based on studies on solvent isotope and viscosity effects (11).

Since the distal heme cavity collapsed upon elimination of R232 by alanine (Fig. 8A and S4A) we cannot provide clear evidence about its role in heterolytic cleavage of hydrogen peroxide. In Compound 0 the hydroperoxyl anion must replace W1 (Fig. 7). As a consequence the positively charged guanidinium group comes close to the distal oxygen atom and will electrostatically promote the heterolysis of the O-O bond to form Compound I. The importance of this transient interaction is difficult to evaluate since the heme architecture collapsed in R232A.

It has to be noted that in the absence of both D143 and R232 Compound I formation still occurred, albeit more than 3 orders of magnitude slower. Substitution of the catalytically relevant histidine and arginine in HRP decreases the rate of Compound I formation by a factor of 10^6 and 10^4 , respectively, but did not abolish it ($k_{app} \sim 20 \text{ M}^{-1}\text{s}^{-1}$ and $3 \times 10^3 \text{ M}^{-1}\text{s}^{-1}$) (37,38). The same was observed for cytochrome *c* peroxidase, where similar mutations reduced Compound I formation by a factor of 10^5 ($k_{app} \sim 300 \text{ M}^{-1}\text{s}^{-1}$) and 10^2 ($k_{app} \sim 3 \times 10^3 \text{ M}^{-1}\text{s}^{-1}$) (39,40), respectively. Slow Compound I formation in the absence of potential distal catalytic residues has also been described recently in the structurally and evolutionary related HemQ from *Listeria monocytogenes* which catalyses the H_2O_2 -mediated decarboxylation of coproheme to heme *b*. However, the mechanism of Compound I formation in HemQ is unknown (41).

In any case Compound I of *KpDyP* is very stable as reflected by the absence of spectral shifts

within minutes. No internal electron transfer reactions occur, which in other heme peroxidases lead to Compound I* formation with typical oxoiron(IV)-type Compound II spectrum (according to Reaction 3) (42). Compound I stability is also reflected by the very negative reduction potential of the Fe(III)/Fe(II) couple (i.e. -350 mV). Typically, $E^{\circ'}$ values of the Fe(III)/Fe(II) couple strictly correlate with $E^{\circ'}$ values of the catalytically relevant redox couples Compound I/Compound II as well as Compound I/ferric state in heme peroxidases (43-46). The more positive the $E^{\circ'}$ value of the redox couple Fe(III)/Fe(II) is (ranging from -350 mV to +50 mV) (20), the more unstable and reactive is Compound I of the respective peroxidase.

In case of wild-type *KpDyP* the extraordinary stability of Compound I strictly correlates with very poor peroxidase activities. Within physiological (i.e. cytosolic) pH regimes (pH 5.0-8.0) Compound I of this cytosolic peroxidase did not react with two-electron donors like chloride or bromide, and to a limited extent with iodide. Only thiocyanate induced a direct but very slow conversion to the ferric resting state (k_4). Halides and thiocyanate typically bind at the distal heme side of peroxidases close to the oxoiron(IV) oxygen of Compound I (47). Importantly, the corresponding two-electron reduction potential of thiocyanate is low (560 mV) (48). Thus, the poor reactivity of *KpDyP* Compound I cannot be argued by thermodynamic reasons only. In addition the restricted accessibility via the small distal access channel might contribute to the observed poor reaction rates. This is supported by the fact that in D143A Compound I the reduction rate of thiocyanate was significantly enhanced due to both higher reactivity and unhampered access as indicated by the crystal structure of D143A.

Finally, for the first time we could identify spectroscopically the formation of an oxoiron(IV)-type Compound II in a B-class DyP with typical absorbance maxima at 418 nm, 527 and 553 nm, when Compound I was mixed with serotonin as one-electron donor. This is in contrast to other reports on redox intermediates of the peroxidase cycle of B-class DyPs (11). Due to very poor activities (or spectral interference) observed with most conventional peroxidase substrates, serotonin was selected. Due to its low standard reduction potential of 650 mV (49) oxidation of serotonin by Compound I (k_5) is typically very fast with all so far studied

heme peroxidases from other superfamilies (50). The fact that in B-class DyPs serotonin is a poor electron donor indicates that neither access channel provides optimal binding and oxidation sites for aromatic substrates. Around neutral pH Compound II did not fully accumulate during steady-state oxidation of serotonin but was clearly visible by the characteristic absorbance bands at 527 and 553 nm. This suggests similar rates of serotonin-mediated Compound I (k_5) and Compound II reduction (k_6). Interestingly, and similarly to SCN⁻ oxidation (k_4), D143A Compound I reduction was several orders of magnitude faster compared to the wild-type enzyme. Both the wild-type and D143A crystal structures show an almost identical heme access via the broad channel leading to propionate p6. However, elimination of D143 opens the entrance to the distal cavity, probably facilitating substrate access to the heme moiety. In any case, during turnover of D143A Compound II accumulated suggesting Compound I reduction rates being significantly higher than Compound II reduction rates ($k_5 > k_6$) in this variant.

In conclusion, heterolytic cleavage of hydrogen peroxide or binding of cyanide by *KpDyP* is pH-independent, very fast and initiated by rate-limiting Compound 0 formation. The fully conserved distal aspartate is responsible for deprotonation of H₂O₂, whereas arginine 232 is important for maintaining the distal heme cavity architecture and might support heterolysis of the O-O bond by transiently and electrostatically interacting with the negatively charged distal oxygen atom. Compound I, an oxoiron(IV) porphyrin radical species, is very stable and only very slowly reacts with two- and one-electron donors. Reduction of Compound I by thiocyanate leads directly to ferric *KpDyP*, whereas reduction by serotonin forms oxoiron(IV)-type Compound II as redox intermediate. Elimination of D143 significantly enhances the reactivity of Compound I with both one- and two-electron donors. Based on our data we challenge the proposal that peroxidase activity towards conventional aromatic substrates or dyes is related to the physiological role of B-class DyPs. At the moment we are not able to answer the question about *in vivo* electron donor(s) of Compound I of B-class DyPs. A study on potential cytosolic interaction partners is in progress.

Experimental procedures

Cloning, Site Directed mutagenesis, Expression and Purification of *KpDyP* and Its Variants. The codon optimized DNA for *KpDyP* was purchased from ATUM (Newark, California) and cloned in frame into pGEX-6P1 using Gibson Assembly kit (New England Biolabs, Ipswich, Ma, USA) and primers 5'-TCAGTCACGATGCGGCCGCTCGATCAACCGAGCGCTTGAAT-ACGCTC-3' and 5'-TCCAGGGGCCCCCTGGGAATGAGCCAAGTACAGAGCGGT-3' for protein production using the GSTrap system. The variants were created by site-directed mutagenesis using the quick change lightning kit (Agilent Technologies, Santa Clara, CA, USA) according to the manufacturers description and primers 5'-GTCTGGTTTCGTGGCCGGCACCG-AGAACC-3' and 5'-GGTTCTCGGTGCCGGCCACGAAACCAGAC-3' for D143A, 5'-GGCCTGAAGATTGTGGCCAGAGCTTGCCGTA-3' and 5'-TACGGCAAGCTCTGGGCCACAA-TCTTCAGGCC-3' for R232A and the combination of both primer sets for the double variant.

The recombinant proteins were expressed heterologously in *E. coli* BL21 (DE3) carrying the pLysS plasmid (Merck/Novagen, Darmstadt, Germany) in Luria Broth supplemented with ampicillin and chloramphenicol. Cells were incubated at 37 °C and 180 rpm until OD₆₀₀ = 0.8, then the cultivation temperature was reduced to 16 °C. Protein expression was induced after one hour using 0.5 mM isopropyl-β-D-thiogalactopyranoside (IPTG) (final concentration) and after 16 hrs growth at 16 °C cells were harvested by centrifugation (4500 rpm, 25 min, 4 °C) and stored at -30 °C.

For protein purification cell pellets were thawed in lysis buffer (50 mM Tris-HCl, pH 7.3, 150 mM NaCl, 0.1% Triton X) with 1 mM PMSF and 100 μM hemin (final concentration). Cells were lysed by sonication (Vibra Cell, Sonics & Materials Inc., Danbury, CT, USA; 50% power, 3 × 60 s) and clarified by centrifugation (18000 rpm, 25 min, 4 °C). The cleared lysate was filtered (0.45 μm, Milipore) and loaded onto a GSTrap HP 5 mL (GE Healthcare) column pre-equilibrated with binding buffer (50 mM Tris-HCl, pH 7.3, 150 mM NaCl). The loaded columns were washed with binding buffer and pre-equilibrated with cleavage buffer (50 mM Tris-HCl, pH 7.0, 150 mM NaCl). For on-column cleavage, columns were manually loaded

with GST-tagged HRV 3C protease diluted in 5 mL cleavage buffer and incubated overnight at 4 °C. Elution was performed with 5 mL cleavage buffer. The eluted protein solution was concentrated using 50 mL Amicon centrifugation units (30 kDa cutoff). The concentrated protein was applied to a HiLoad 16/60 Superdex 200 prep grade column (GE Healthcare), pre-equilibrated with 50 mM phosphate buffer, pH 7.0, and collected in 500 μ L fractions. All fractions with a RZ-value higher than 1.9 for the wild-type protein and the D143A variant and 2.5 for the variants R232A and D143A/R232A were collected, concentrated to higher than 500 μ M, aliquoted and stored at -80 °C.

UV-vis and Circular Dichroism Spectroscopy. All UV-vis spectra were measured at room temperature on a Hitachi U-3900 spectrometer. For each measurement, 1000 μ L of KpDyP with a concentration of 10 μ M were prepared in 50 mM phosphate buffer (pH 7.0) and used for UV-vis analysis. For all experiments involving a comparison between pH 4.0 and 8.0 50 mM phosphate citrate buffer was used and between pH 8.0 and 10.0 50 mM Glycine NaOH was used.

For secondary structure prediction electronic circular dichroism (ECD) spectra were taken in the far-UV (180 nm- 260 nm) using Chirscan from Applied Photophysics (Leatherhead, UK), the bandwidth was set to 3 mm, pathlength was 1 mm and scan speed was 10 s nm⁻¹. The instrument was flushed with nitrogen at a flow rate of 5 L min⁻¹ and allowed simultaneous UV-vis and ECD monitoring. Samples (400 μ L enzyme solution (10 μ M) in 5 mM phosphate buffer (pH 7.0) were measured at RT. For ECD spectra in the near-UV and visible ranges (260 nm to 450 nm) the bandwidth was set to 3 mm, pathlength was 10 mm and the scan speed was 5 s nm⁻¹. Samples consisted of 1 mL enzyme solution (10 μ M) in 50 mM phosphate buffer (pH 7.0).

Electron Paramagnetic Resonance. For electron paramagnetic resonance (EPR) spectroscopic studies, 500 μ M protein was prepared in 50 mM phosphate buffer, pH 7.0. In all cases, 30% glycerol was added as a cryoprotectant. Typically, 100 μ L was inserted in a quartz EPR tube and flash frozen in liquid N₂. In addition, the wild-type protein was activated by adding a 5-fold molar excess of H₂O₂ to generate Compound I. The EPR sample tubes were vacuum-pumped to 1 mbar during the experiments to remove excess of paramagnetic

dioxygen. X-band continuous-wave (CW) EPR experiments were performed on a Bruker ESP300E spectrometer operating at a microwave frequency of ca. 9.44 GHz equipped with a liquid-helium cryostat (Oxford Inc.) to enable temperatures from 2.5 K up to room temperature. Calibration of the magnetic field was done using a Bruker ER035M NMR Gaussmeter.

All spectra of the ferric proteins were recorded at 4 K under non-saturating conditions at 1 mW microwave power and 0.5 mT modulation amplitude. The detailed EPR spectrum of the organic radical in the resting state protein was recorded at 80 K using 0.1 mW microwave power and 1 mT modulation amplitude. The EPR spectrum of compound I was recorded at 2.5 K using 100 μ W microwave power and 0.1 mT modulation amplitude. In all cases, the modulation frequency was 100 kHz. Simulation of the experimental spectra was done using the Matlab (MathWorks, Natick, MA, USA)-based software Easyspin (51).

Differential Scanning Calorimetry. Temperature-induced pH-dependent protein unfolding studies were performed using differential scanning calorimetry (DSC). All samples were analyzed between 20–100 °C. Samples were heated at 60 psi (4.136 bar) with a rate of 60 °C h⁻¹ cell pressure using a VP-capillary DSC microcalorimeter from Microcal (cell volume: 137 μ L), equipped with an autosampler for 96 well plates. All samples consisted of 10 μ M enzyme in 50 mM phosphate-citrate buffer, pH 3.0 -7.5 (wild-type) and pH 4.5 - 7.5 (variants) and were kept at 4 °C before measurement. Collected data were corrected for buffer baseline, normalized for protein concentration and analyzed using the Microcal origin software package.

Spectroelectrochemistry. The standard reduction potential, E° , of the Fe(III)/Fe(II) couple was determined using a homemade OTTLE cell (43,52-54). The three-electrode configuration consisted of a gold minigrad working electrode (Buckbee-Mears), a homemade Ag/AgCl/KCl_{sat} microreference electrode, separated from the working solution by a Vycor set, and a platinum wire as the counter electrode (43,52-54). The reference electrode was calibrated against a saturated calomel (HgCl) electrode before each set of measurements. All potentials are referenced to the standard hydrogen electrode (SHE, +242 mV). Potentials were applied across the OTTLE cell with an Amel

model 2053 potentiostat/galvanostat. A constant temperature was maintained by a circulating water bath and the OTTLE cell temperature was monitored with a copper-costan microthermo-couple. UV-vis spectra were recorded using a Varian Cary C50 spectrophotometer (Agilent Technologies, Santa Clara, CA, USA). The OTTLE cell was flushed with argon gas to establish an oxygen-free environment in the cell. Spectroelectrochemical titrations were performed with 15 μM wild-type KpDyP or mutants in 100 mM sodium phosphate buffer (pH 7.0) plus 100 mM NaCl. Additionally, 25 μM methyl viologen and 1 μM lumiflavin 3-acetate, methylene blue, phenazine methosulfate, and indigo disulfonate were used as redox mediators.

Steady-state and Transient-State Kinetics. Substrate specificity was determined by following the increase or decrease of absorbance at specified wavelengths for 120 s using a stirred cuvette and a scanning photometer (Hitachi U-3900, Tokyo, Japan). A typical reaction consisted of 1 mL 50 mM phosphate-citrate buffer, pH 4.0 to pH 7.0, with 100 μM , 1 mM or 10 mM substrate, 500 μM H_2O_2 and 200 nM enzyme. All reactions were carried out in triplicates.

All transient-state experiments were conducted with stopped-flow apparatus (SX-18MV or pi-star fitted equipped with diode array detector or a monochromator) from Applied Photophysics. The optical quartz cell with a path length of 10 mm had a volume of 20 μL . The fastest time for mixing was 0.68 ms, all measurements were performed at 25 $^\circ\text{C}$. For single wavelength measurements a minimum of three runs were performed for each ligand or substrate concentration. Typically, in studies of the kinetics of formation of the KpDyP-cyanide complex 2 μM of ferric protein in 50 mM phosphate buffer, pH 7.0, was mixed with at least a 10-fold excess of cyanide in the same buffer. The reaction was monitored by following the increase of absorbance at 420 nm. For studies on the pH-dependence of cyanide binding, 2 μM enzyme in 5 mM phosphate citrate buffer, pH 7.0, was mixed with at least 10-fold excess of cyanide in 100 mM phosphate-citrate buffer, pH 3.0 to 8.0, or 100 mM glycine-NaOH buffer, pH 8.0-10.0.

In addition to elucidation of the kinetics of cyanide binding to ferric B-class DyP the thermodynamics of the low-spin complex formation was investigated. In detail, for ligand titration 1 mL of 5-10 μM protein was prepared in 50 mM

phosphate buffer, pH 7.0. The titrations were performed in a stirred cuvette at 25 $^\circ\text{C}$ and monitored by UV-vis absorption spectroscopy between 250 and 700 nm using a scanning photometer (Hitachi U-3900, Tokyo, Japan). Cyanide was added stepwise from a 1 M stock solution. All spectra were corrected for the dilution and smoothed using Savitzky-Golay smoothing algorithm provided by the Hitachi U-3900 software package.

For studying the kinetics of Compound I formation the conventional stopped-flow mode was used. In a typical experiment 2 μM of ferric enzyme in 50 mM phosphate buffer, pH 7.0, was mixed with at least a 10-fold excess of H_2O_2 in the same buffer. The pH dependency of this reaction was measured with 2 μM enzyme in 5 mM phosphate citrate buffer, pH 7.0, mixed with at least 10-fold excess of hydrogen peroxide in 100 mM phosphate citrate buffer, pH 3.0 to 8.0, or 100 mM glycine NaOH buffer, pH 8.0-10.0.

For studying the reactivity of wild-type KpDyP and the variant D143A Compound I with the two-electron donor thiocyanate and the one-electron donor serotonin the sequential stopped-flow mode was used. In detail, Compound I was formed by mixing 2 μM ferric wild-type KpDyP with a two-fold stoichiometric excess of hydrogen peroxide in 50 mM phosphate buffer, pH 7.0. After a delay-time of 100 ms Compound I was mixed with varying concentrations of thiocyanate or serotonin. In case of the D143A variant Compound I was preformed by mixing 2 μM D143A with a 500-fold excess of H_2O_2 and the delay time was 3000 ms.

Crystallization and Structure Determination. All enzymes crystallized in optimized conditions of SG1 Screen HT-96 (Molecular Dimensions, Newmarket, UK) well C9. Crystallization experiments were performed using SWISSCI MRC three-well crystallization plates (Molecular Dimensions, Newmarket, UK) adopting the vapor diffusion method. Crystallization drops were set using a Mosquito LCP (TTP Labtech, Melbourn Science Park, Melbourn, UK). All protein stocks were prepared in a final concentration of 8.25 $\text{mg}\cdot\text{mL}^{-1}$ in 50 mM phosphate buffer, pH 7.0. The seed solution was prepared by collecting all crystals of a single well in 50 μL 50 mM phosphate buffer, pH 7.0, containing ten 1.0 mm glass beads followed by pulverization through 4 \times 1 min vortexing at full speed. The initial seed stock was diluted depending on the amount of crystals used. The reservoir was

filled with 40 μ L crystallization solution. Crystallization drops were set up with enzyme: seed: crystallization solution ratios of 100 : 100 : 200 nL, 200 : 100 : 200 nL, and 300 : 100 : 200 nL. Crystallization plates were stored at 22 °C.

Wild-type KpDyP crystallized in 23% w/v PEG 3350, 0.1 M MgCl₂, 0.1 M Tris-HCl, pH 8.5, the D143A variant in 23% w/v PEG 3350, 0.1 M MgCl₂, 0.1 M Tris-HCl, pH 8.5, R232A in 29% w/v PEG 3350, 0.15 M MgCl₂, 0.1 M Tris-HCl, pH 8.5, and D143A/R232A in 23% w/v PEG 3350, 0.1 M MgCl₂, 0.1 M Tris-HCl, pH 8.5, 5% w/v glycerol. For cryo-protection the crystallization conditions were supplemented with 25% w/v glycerol. All crystals were harvested using cryo-loops, and flash-vitrified in liquid nitrogen.

Datasets were collected at beam-line ID30A-1 (55) of the European Synchrotron Radiation Facility (ESRF, Grenoble, France) at 100 K using a PILATUS3 2M Detector or at beamline I24 of the Diamond Light Source (Harwell Science and Innovation Campus, Didcot, England) at 100 K using Pilatus3 6M Detector. The datasets were processed with XDS using xia2 as part of the CCP4 v7.0 Program Suite (56-58). The phase problem was solved by molecular replacement using Phaser-MR taking PDB structure 5de0, DyP type-B from *V. cholerae* (10) or the wild-type KpDyP structure

described here. The models were further improved by iterative cycles of manual model building using coot (59) and maximum likelihood refinement using PHENIX-Refine (60). PHENIX-refine converts intensities into amplitudes using the French and Wilson algorithm (61). Final stages of refinement included Translation Liberation Screw (TLS) parameters (for R232A) or anisotropic refinement of all atoms (for wild-type KpDyP and D143A/R232A), isotropic B-factor model, automated addition of hydrogens and water molecules, optimization of X-ray/ADP weight, and optimization of X-ray/stereochemistry weight. The model was validated with MolProbity (62,63), the final resolution cutoff was determined using paired refinement with PDB-REDO (64). Metal coordination was validated using the CheckMyMetal web server (www.csgid.org/csgid/metal_sites) (65,66). Figures were prepared with pymol (<http://www.pymol.org>). Atomic coordinates have been deposited in the Protein Data Bank under accession code 6FKS, 6FL2, 6FKT and 6FIY. Dimensions of putative access channels were calculated using the pymol plugin CAVER 3.0.1. To calculate the access channel the heme iron position was used as starting coordinates and heme was excluded. Minimum probe radius was 0.9, shell depth was set to 10 and shell radius to 9.

Acknowledgements: This project was supported by the Austrian Science Fund, FWF [Doctoral Program BioToP - Molecular Technology of Proteins (W1224)] and by the FWO/FWF lead agency grant (G005416N). The authors would like to thank Diamond Light Source for beamtime (proposal mx16011), and the staff of beamline I24 for assistance with crystal testing and data collection. The authors acknowledge the support and the use of resources of Instruct-ERIC.

Conflict of interest: The authors declare that they have no conflict of interest with the contents of this work.

References

1. Kim, S. J., and Shoda, M. (1999) Decolorization of molasses and a dye by a newly isolated strain of the fungus *Geotrichum candidum* Dec 1. *Biotechnol Bioeng* **62**, 114-119
2. Sugano, Y., Nakano, R., Sasaki, K., and Shoda, M. (2000) Efficient heterologous expression in *Aspergillus oryzae* of a unique dye-decolorizing peroxidase, DyP, of *Geotrichum candidum* Dec 1. *Appl Environ Microbiol* **66**, 1754-1758
3. Sugano, Y., Muramatsu, R., Ichiyanaagi, A., Sato, T., and Shoda, M. (2007) DyP, a Unique Dye-decolorizing Peroxidase, Represents a Novel Heme Peroxidase Family: Asp171 replaces the distal histidine of classical peroxidases. *J Biol Chem* **282**, 36652-36658
4. Zámocký, M., Hofbauer, S., Schaffner, I., Gasselhuber, B., Nicolussi, A., Souidi, M., Pirker, K. F., Furtmüller, P. G., and Obinger, C. (2015) Independent evolution of four heme peroxidase superfamilies. *Arch Biochem Biophys* **574**, 108-119
5. Yoshida, T., and Sugano, Y. (2015) A structural and functional perspective of DyP-type peroxidase family. *Arch Biochem Biophys* **574**, 49-55
6. Roberts, J. N., Singh, R., Grigg, J. C., Murphy, M. E. P., Bugg, T. D. H., and Eltis, L. D. (2011) Characterization of Dye-Decolorizing Peroxidases from *Rhodococcus jostii*RHA1. *Biochemistry* **50**, 5108-5119
7. Singh, R., Grigg, J. C., Armstrong, Z., Murphy, M. E., and Eltis, L. D. (2012) Distal heme pocket residues of B-type dye-decolorizing peroxidase: arginine but not aspartate is essential for peroxidase activity. *J Biol Chem* **287**, 10623-10630
8. Mendes, S., Brissos, V., Gabriel, A., Catarino, T., Turner, D. L., Todorovic, S., and Martins, L. O. (2015) An integrated view of redox and catalytic properties of B-type PpDyP from *Pseudomonas putida* MET94 and its distal variants. *Arch Biochem Biophys* **574**, 99-107
9. Letoffe, S., Heuck, G., Delepelaire, P., Lange, N., and Wandersman, C. (2009) Bacteria capture iron from heme by keeping tetrapyrrol skeleton intact. *Proc Natl Acad Sci U S A* **106**, 11719-11724
10. Uchida, T., Sasaki, M., Tanaka, Y., and Ishimori, K. (2015) A Dye-Decolorizing Peroxidase from *Vibrio cholerae*. *Biochemistry* **54**, 6610-6621
11. Shrestha, R., Huang, G., Meekins, D. A., Geisbrecht, B. V., and Li, P. (2017) Mechanistic Insights into Dye-Decolorizing Peroxidase Revealed by Solvent Isotope and Viscosity Effects. *ACS Catal* **7**, 6352-6364
12. Ahmad, M., Roberts, J. N., Hardiman, E. M., Singh, R., Eltis, L. D., and Bugg, T. D. H. (2011) Identification of DypB from *Rhodococcus jostii*RHA1 as a Lignin Peroxidase. *Biochemistry* **50**, 5096-5107
13. Singh, R., Grigg, J. C., Qin, W., Kadla, J. F., Murphy, M. E., and Eltis, L. D. (2013) Improved manganese-oxidizing activity of DypB, a peroxidase from a lignolytic bacterium. *ACS Chem Biol* **8**, 700-706
14. Dailey, H. A., Septer, A. N., Daugherty, L., Thames, D., Gerdes, S., Stabb, E. V., Dunn, A. K., Dailey, T. A., and Phillips, J. D. (2011) The *Escherichia coli* protein YfeX functions as a porphyrinogen oxidase, not a heme dechelataase. *MBio* **2**, e00248-00211
15. Poulos, T. L., and Kraut, J. (1980) The stereochemistry of peroxidase catalysis. *J Biol Chem* **255**, 8199-8205
16. Poulos, T. L., Freer, S. T., Alden, R. A., Edwards, S. L., Skogland, U., Takio, K., Eriksson, B., Xuong, N., Yonetani, T., and Kraut, J. (1980) The crystal structure of cytochrome c peroxidase. *J Biol Chem* **255**, 575-580
17. Chen, C., Shrestha, R., Jia, K., Gao, P. F., Geisbrecht, B. V., Bossmann, S. H., Shi, J., and Li, P. (2015) Characterization of Dye-decolorizing Peroxidase (DyP)

- from *Thermomonospora curvata* Reveals Unique Catalytic Properties of A-type DyPs. *J Biol Chem* **290**, 23447-23463
18. Fitch, C. A., Platzer, G., Okon, M., Garcia-Moreno, B. E., and McIntosh, L. P. (2015) Arginine: Its pKa value revisited. *Protein Sci* **24**, 752-761
 19. Barr, I., and Guo, F. (2015) Pyridine Hemochromagen Assay for Determining the Concentration of Heme in Purified Protein Solutions. *Bio Protoc* **5**
 20. Weil, J. A. a. B., J.R. (2006) *Electron Paramagnetic Resonance, 2nd ed.*, Wiley, Hoboken, NJ
 21. Lendzian, F. (2005) Structure and interactions of amino acid radicals in class I ribonucleotide reductase studied by ENDOR and high-field EPR spectroscopy. *Biochim Biophys Acta* **1707**, 67-90
 22. Linde, D., Pogni, R., Canellas, M., Lucas, F., Guallar, V., Baratto, M. C., Sinicropi, A., Saez-Jimenez, V., Coscolin, C., Romero, A., Medrano, F. J., Ruiz-Duenas, F. J., and Martinez, A. T. (2015) Catalytic surface radical in dye-decolorizing peroxidase: a computational, spectroscopic and site-directed mutagenesis study. *Biochem J* **466**, 253-262
 23. Schrestha, R., Chen, X., Ramyar, K.X., Hayati, Z., Carlson, E.A., Bossmann, S.H., Song, L., Geisbrecht, B.V. and Li, P. (2016) Identification of surface-exposed protein radicals and a substrate oxidation site in A-class dye-decolorizing peroxidase from *Thermomonospora curvata*. *ACS Catal* **6**, 8036-8047
 24. Baratto, M. C., Sinicropi, A., Linde, D., Sáez-Jiménez, V., Sorace, L., Ruiz-Duenas, F. J., Martinez, A. T., Basosi, R., and Pogni, R. (2015) Redox-Active Sites in *Auricularia auricula-judae* Dye-Decolorizing Peroxidase and Several Directed Variants: A Multifrequency EPR Study. *J Phys Chem B* **119**, 13583-13592
 25. Strittmatter, E., Serrer, K., Liers, C., Ullrich, R., Hofrichter, M., Piontek, K., Schleicher, E., and Plattner, D. A. (2015) The toolbox of *Auricularia auricula-judae* dye-decolorizing peroxidase - Identification of three new potential substrate-interaction sites. *Arch Biochem Biophys* **574**, 75-85
 26. Nakajima, R., and Yamazaki, I. (1980) The conversion of horseradish peroxidase C to a verdohemoprotein by a hydroperoxide derived enzymatically from indole-3-acetic acid and by m-nitroperoxybenzoic acid. *J Biol Chem* **255**, 2067-2071
 27. Aasa, R., Vanngard, T., and Dunford, H. B. (1975) EPR studies on compound I of horseradish peroxidase. *Biochim Biophys Acta* **391**, 259-264
 28. Schulz, C. E., Devaney, P. W., Winkler, H., Debrunner, P. G., Doan, N., Chiang, R., Rutter, R., and Hager, L. P. (1979) Horseradish peroxidase compound I: evidence for spin coupling between the heme iron and a 'free' radical. *FEBS Lett* **103**, 102-105
 29. Svistunenko, D. A., Worrall, J.A.R., Chugh, S.B., Haigh, S.C., Ghiladi, R.A. and Nicholls, P. (2012) Ferric haem forms of *Mycobacterium tuberculosis* catalase-peroxidase probed by EPR spectroscopy: Their stability and interplay with pH. *Biochimie* **94**, 1274-1280
 30. Freire, D. M., Rivas, M.G., Dias, A.M., Lopes, A.T., Costa, C., Santos-Silva, T., Van Doorslaer, S. and Gonzalez, P.J. (2015) The homopentameric chlorite dismutase from *Magnetospirillum* sp. *Journal of Inorganic Biochemistry* **151**, 1-9
 31. De Schutter, A., Correia, H.D., Freire, D.M., Rivas, M.G., Rizzi, A., Santos-Silva, T., Gonzalez, P.J. and Van Doorslaer, S. (2015) Ligand binding to chlorite dismutase from *Magnetospirillum* sp. *J Phys Chem B* **119**, 13859-13869
 32. Schaffner, I., Hofbauer, S., Krutzler, M., Pirker, K.F., Bellei, M., Stadlmayr, G., Mlynek, G., Djinovic-Carugo, K., Battistuzzi, G., Furtmuller, P.G., Daims, H. and Obinger, C. (2015)

- Dimeric chlorite dismutase from the nitrogen-fixing cyanobacterium *Cyanothece* sp. PCC7425. *Mol Microbiol* **96**, 1053-1068
33. Linde, D., Pogni, R., Canellas, M., Lucas, F., Guallar, V., Baratto, M.C., Sinicropi, A., Saez-Jimenez, V., Coscolin, C., Romero, A., Medrano, F.J., Ruiz-Duenas, F.J. and Martinez, A.T. (2015) Catalytic surface radical in dye-decolorizing peroxidase: a computational, spectroscopic and site-directed mutagenesis study. *Biochem J* **466**, 253-262
 34. Roberts, J. N., Singh, R., Grigg, J.C., Murphy, M.E.P., Bugg, T. D. H. and Eltis, L. (2011) Characterization of dye-decolorizing peroxidases from *Rhodococcus jostii* RHA1. *Biochemistry* **50**, 5108-5119
 35. Jones, P., and Dunford, H. B. (2005) The mechanism of Compound I formation revisited. *J Inorg Biochem* **99**, 2292-2298
 36. Branchaud, B. P. (2000) Heme Peroxidases By H. Brian Dunford (University of Alberta). Wiley-VCH, John Wiley and Sons: New York. 1999. xi + 507 pp. \$195.00. ISBN 0-471-24244-6. *J Am Chem Soc* **122**, 7434-7434
 37. Newmyer, S. L., and Ortiz de Montellano, P. R. (1995) Horseradish peroxidase His-42 --> Ala, His-42 --> Val, and Phe-41 --> Ala mutants. Histidine catalysis and control of substrate access to the heme iron. *J Biol Chem* **270**, 19430-19438
 38. Rodriguez-Lopez, J. N., Smith, A. T., and Thorneley, R. N. (1996) Role of arginine 38 in horseradish peroxidase. A critical residue for substrate binding and catalysis. *J Biol Chem* **271**, 4023-4030
 39. Vitello, L. B., Erman, J. E., Miller, M. A., Wang, J., and Kraut, J. (1993) Effect of arginine-48 replacement on the reaction between cytochrome c peroxidase and hydrogen peroxide. *Biochemistry* **32**, 9807-9818
 40. Erman, J. E., Vitello, L. B., Miller, M. A., Shaw, A., Brown, K. A., and Kraut, J. (1993) Histidine 52 is a critical residue for rapid formation of cytochrome c peroxidase compound I. *Biochemistry* **32**, 9798-9806
 41. Hofbauer, S., Mlynek, G., Milazzo, L., Puhlinger, D., Maresch, D., Schaffner, I., Furtmuller, P. G., Smulevich, G., Djinojic-Carugo, K., and Obinger, C. (2016) Hydrogen peroxide-mediated conversion of coproheme to heme b by HemQ-lessons from the first crystal structure and kinetic studies. *FEBS J* **283**, 4386-4401
 42. Vlasits, J., Jakopitsch, C., Bernroitner, M., Zamocky, M., Furtmuller, P. G., and Obinger, C. (2010) Mechanisms of catalase activity of heme peroxidases. *Arch Biochem Biophys* **500**, 74-81
 43. Battistuzzi, G., Bellei, M., Bortolotti, C. A., and Sola, M. (2010) Redox properties of heme peroxidases. *Arch Biochem Biophys* **500**, 21-36
 44. Battistuzzi, G., Stampfer, J., Bellei, M., Vlasits, J., Soudi, M., Furtmuller, P. G., and Obinger, C. (2011) Influence of the covalent heme-protein bonds on the redox thermodynamics of human myeloperoxidase. *Biochemistry* **50**, 7987-7994
 45. Paumann-Page, M., Katz, R. S., Bellei, M., Schwartz, I., Edenhofer, E., Sevcnikar, B., Soudi, M., Hofbauer, S., Battistuzzi, G., Furtmuller, P. G., and Obinger, C. (2017) Pre-steady-state Kinetics Reveal the Substrate Specificity and Mechanism of Halide Oxidation of Truncated Human Peroxidase 1. *J Biol Chem* **292**, 4583-4592
 46. Nicolussi, A., Auer, M., Weissensteiner, J., Schutz, G., Katz, S., Maresch, D., Hofbauer, S., Bellei, M., Battistuzzi, G., Furtmuller, P. G., and Obinger, C. (2017) Posttranslational Modification of Heme b in a Bacterial Peroxidase: The Role of Heme to Protein Ester Bonds in Ligand Binding and Catalysis. *Biochemistry* **56**, 4525-4538

47. Zederbauer, M., Furtmuller, P. G., Brogioni, S., Jakopitsch, C., Smulevich, G., and Obinger, C. (2007) Heme to protein linkages in mammalian peroxidases: impact on spectroscopic, redox and catalytic properties. *Nat Prod Rep* **24**, 571-584
48. Arnhold, J., Monzani, E., Furtmüller, P. G., Zederbauer, M., Casella, L., and Obinger, C. (2006) Kinetics and Thermodynamics of Halide and Nitrite Oxidation by Mammalian Heme Peroxidases. *Eur J Inorg Chem* **2006**, 3801-3811
49. Sarada, B. V., Rao, T. N., Tryk, D. A., and Fujishima, A. (2000) Electrochemical oxidation of histamine and serotonin at highly boron-doped diamond electrodes. *Anal Chem* **72**, 1632-1638
50. Jantschko, W., Furtmuller, P. G., Allegra, M., Livrea, M. A., Jakopitsch, C., Regelsberger, G., and Obinger, C. (2002) Redox intermediates of plant and mammalian peroxidases: a comparative transient-kinetic study of their reactivity toward indole derivatives. *Arch Biochem Biophys* **398**, 12-22
51. Stoll, S., and Schweiger, A. (2006) EasySpin, a comprehensive software package for spectral simulation and analysis in EPR. *J Magn Reson* **178**, 42-55
52. Battistuzzi, G., Bellei, M., Vlasits, J., Banerjee, S., Furtmuller, P. G., Sola, M., and Obinger, C. (2010) Redox thermodynamics of lactoperoxidase and eosinophil peroxidase. *Arch Biochem Biophys* **494**, 72-77
53. Battistuzzi, G., Bellei, M., Zederbauer, M., Furtmuller, P. G., Sola, M., and Obinger, C. (2006) Redox thermodynamics of the Fe(III)/Fe(II) couple of human myeloperoxidase in its high-spin and low-spin forms. *Biochemistry* **45**, 12750-12755
54. Battistuzzi, G., Borsari, M., Loschi, L., Menziani, M. C., De Rienzo, F., and Sola, M. (2001) Control of metalloprotein reduction potential: the role of electrostatic and solvation effects probed on plastocyanin mutants. *Biochemistry* **40**, 6422-6430
55. Beteva, A., Cipriani, F., Cusack, S., Delageniere, S., Gabadinho, J., Gordon, E. J., Guijarro, M., Hall, D. R., Larsen, S., Launer, L., Lavault, C. B., Leonard, G. A., Mairs, T., McCarthy, A., McCarthy, J., Meyer, J., Mitchell, E., Monaco, S., Nurizzo, D., Pernot, P., Pieritz, R., Ravelli, R. G., Rey, V., Shepard, W., Spruce, D., Stuart, D. I., Svensson, O., Theveneau, P., Thibault, X., Turkenburg, J., Walsh, M., and McSweeney, S. M. (2006) High-throughput sample handling and data collection at synchrotrons: embedding the ESRF into the high-throughput gene-to-structure pipeline. *Acta Crystallogr D Biol Crystallogr* **62**, 1162-1169
56. Kabsch, W. (2010) Xds. *Acta Crystallogr D Biol Crystallogr* **66**, 125-132
57. Winter, G. (2010) xia2: an expert system for macromolecular crystallography data reduction. *J Appl Crystallogr* **43**, 186-190
58. Winn, M. D., Ballard, C. C., Cowtan, K. D., Dodson, E. J., Emsley, P., Evans, P. R., Keegan, R. M., Krissinel, E. B., Leslie, A. G., McCoy, A., McNicholas, S. J., Murshudov, G. N., Pannu, N. S., Potterton, E. A., Powell, H. R., Read, R. J., Vagin, A., and Wilson, K. S. (2011) Overview of the CCP4 suite and current developments. *Acta Crystallogr D Biol Crystallogr* **67**, 235-242
59. Emsley, P., Lohkamp, B., Scott, W. G., and Cowtan, K. (2010) Features and development of Coot. *Acta Crystallogr D Biol Crystallogr* **66**, 486-501
60. Adams, P. D., Afonine, P. V., Bunkoczi, G., Chen, V. B., Davis, I. W., Echols, N., Headd, J. J., Hung, L. W., Kapral, G. J., Grosse-Kunstleve, R. W., McCoy, A. J., Moriarty, N. W., Oeffner, R., Read, R. J., Richardson, D. C., Richardson, J. S., Terwilliger, T. C., and Zwart, P. H. (2010) PHENIX: a comprehensive Python-based system for macromolecular structure solution. *Acta Crystallogr D Biol Crystallogr* **66**, 213-221

61. French, S., and Wilson, K. (1978) On the treatment of negative intensity observations. *Acta Crystallographica Section A* **34**, 517-525
62. Davis, I. W., Leaver-Fay, A., Chen, V. B., Block, J. N., Kapral, G. J., Wang, X., Murray, L. W., Arendall, W. B., 3rd, Snoeyink, J., Richardson, J. S., and Richardson, D. C. (2007) MolProbity: all-atom contacts and structure validation for proteins and nucleic acids. *Nucleic Acids Res* **35**, W375-383
63. Chen, V. B., Arendall, W. B., 3rd, Headd, J. J., Keedy, D. A., Immormino, R. M., Kapral, G. J., Murray, L. W., Richardson, J. S., and Richardson, D. C. (2010) MolProbity: all-atom structure validation for macromolecular crystallography. *Acta Crystallogr D Biol Crystallogr* **66**, 12-21
64. Joosten, R. P., Long, F., Murshudov, G. N., and Perrakis, A. (2014) The PDB_REDO server for macromolecular structure model optimization. *IUCrJ* **1**, 213-220
65. Zheng, H., Chordia, M. D., Cooper, D. R., Chruszcz, M., Muller, P., Sheldrick, G. M., and Minor, W. (2014) Validation of metal-binding sites in macromolecular structures with the CheckMyMetal web server. *Nat Protoc* **9**, 156-170
66. Zheng, H., Cooper, D. R., Porebski, P. J., Shabalin, I. G., Handing, K. B., and Minor, W. (2017) CheckMyMetal: a macromolecular metal-binding validation tool. *Acta Crystallogr D Struct Biol* **73**, 223-233
67. Blumberg, W. E., Peisach, J., Wittenberg, B. A., and Wittenberg, J. B. (1968) The electronic structure of protoheme proteins. I. An electron paramagnetic resonance and optical study of horseradish peroxidase and its derivatives. *J Biol Chem* **243**, 1854-1862
68. Svistunenko, D. A., Worrall, J. A., Chugh, S. B., Haigh, S. C., Ghiladi, R. A., and Nicholls, P. (2012) Ferric haem forms of Mycobacterium tuberculosis catalase-peroxidase probed by EPR spectroscopy: Their stability and interplay with pH. *Biochimie* **94**, 1274-1280
69. Hofbauer, S., Gruber, C., Pirker, K. F., Sundermann, A., Schaffner, I., Jakopitsch, C., Oostenbrink, C., Furtmuller, P. G., and Obinger, C. (2014) Transiently produced hypochlorite is responsible for the irreversible inhibition of chlorite dismutase. *Biochemistry* **53**, 3145-3157

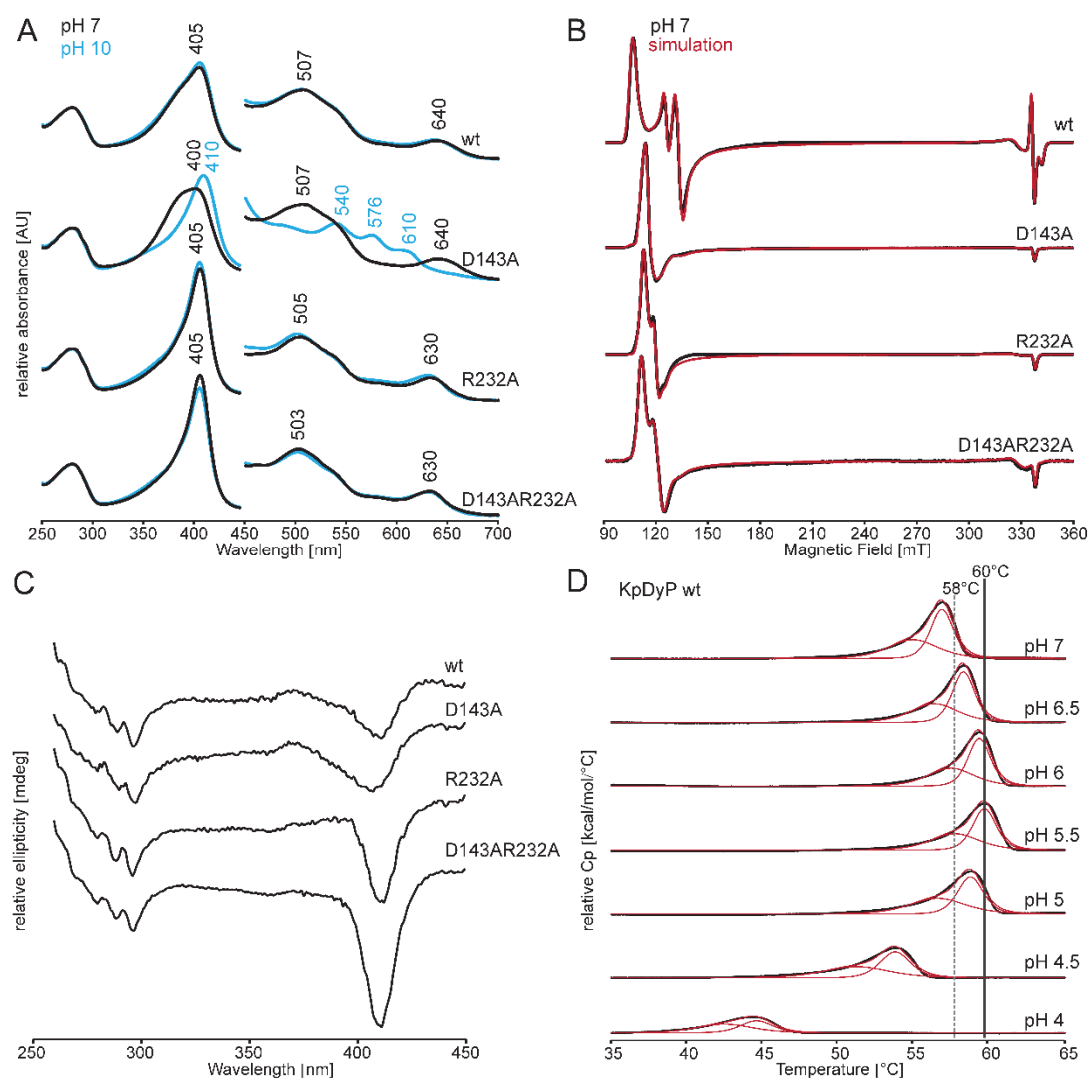


Figure 1. Spectral properties and thermal stabilities of wild-type *KpDyP* and the variants D143A, R232A and D143A/R232A. (A) UV-Vis spectra of wild-type (wt) *KpDyP*, D143A, R232A and D143A/R232A in 50 mM phosphate buffer, pH 7.0 (black) and in 50 mM borate buffer pH 10.0 (blue). (B) Low temperature X-band CW-EPR spectra of wt *KpDyP* and variants in 50 mM phosphate buffer, pH 7.0 (black) and their corresponding spectral simulations (red). (C) Circular dichroism spectra of wild-type *KpDyP* and variants in 50 mM phosphate buffer pH 7.0 in the near UV region (260-450 nm). (D) DSC thermograms of wild-type *KpDyP* between pH 4.0 and 7.0 (black). The corresponding fits using a non-two-state transition model are depicted in red. The highest T_m values (pH 5.5) are highlighted with grey lines.

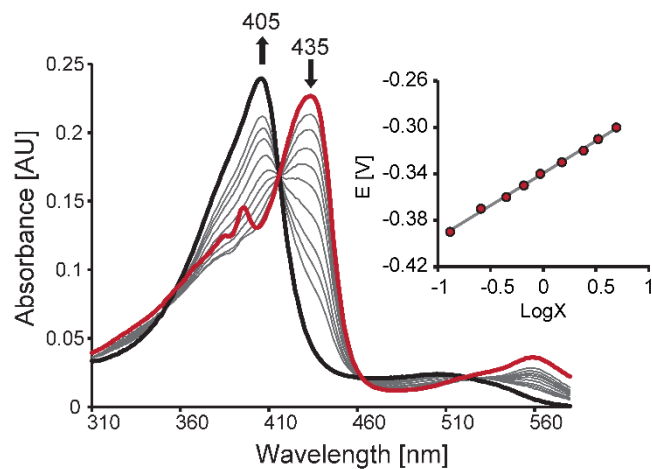


Figure 2. Spectroelectrochemical titration of wild-type *KpDyP*. Electronic absorption spectra of wild-type *KpDyP* at different applied potentials. Bold black spectrum represent fully oxidized, ferric enzyme (Soret maximum at 405 nm) and red spectrum represent fully reduced (Soret maximum at 435 nm) protein. The inset shows the corresponding Nernst plot, where X represents $(A_{\lambda_{\text{redMax}}} - A_{\lambda_{\text{red}}}) / (A_{\lambda_{\text{oxMax}}} - A_{\lambda_{\text{ox}}})$

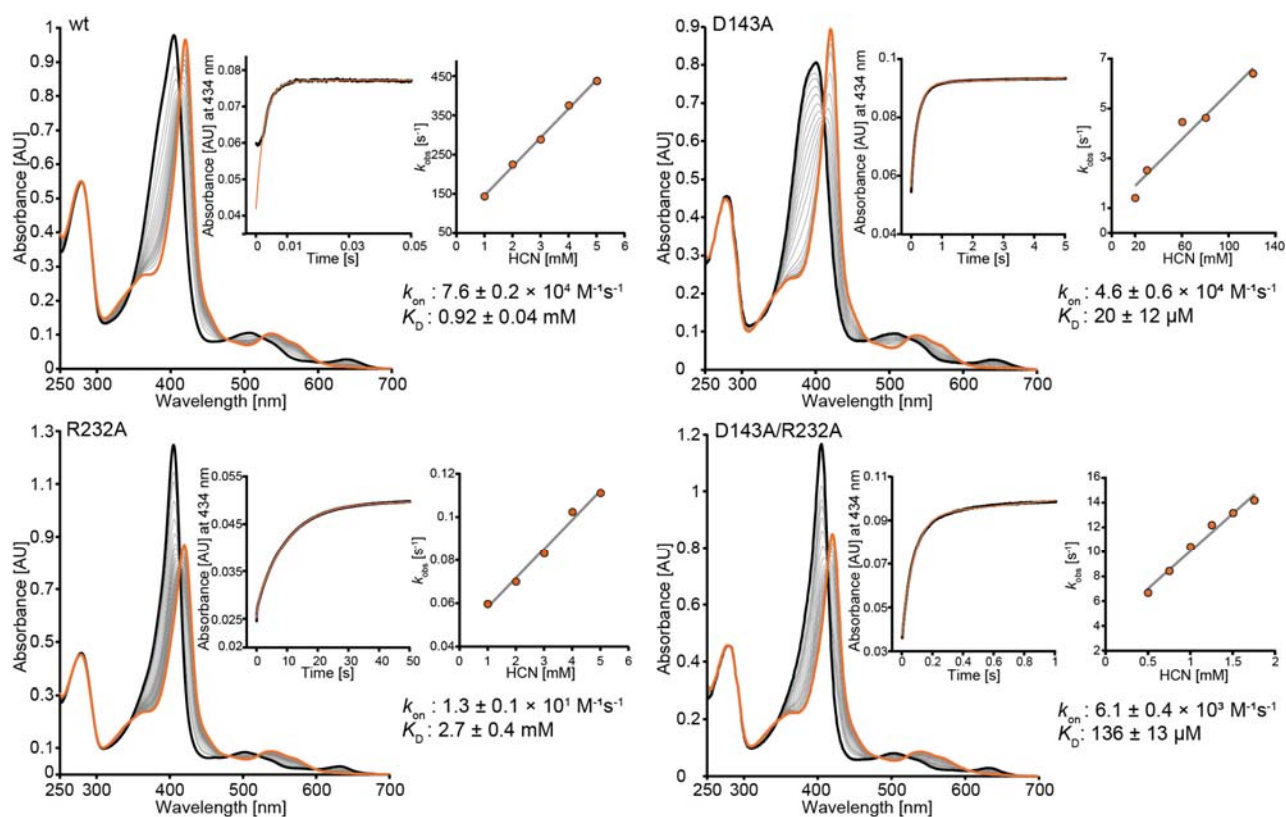


Figure 3. Kinetics of cyanide binding to ferric wild-type *KpDyP* and the variants D143A, R232A and D143A/R232A at pH 7.0. Spectral conversion of high-spin ferric protein (black spectrum) to the corresponding low-spin cyanide complex (orange spectrum). Wild-type (A), D143A (B), R232A (C) and D143A/R232A (D). The insets show representative time traces (black) and fits (orange) at 434 nm (wild-type *KpDyP* : 5 mM, D143A: 100 μ M, R232A: 5 mM, D143A/R232A: 1.5 mM). Additionally, insets show the corresponding linear plots of k_{obs} versus cyanide concentration.

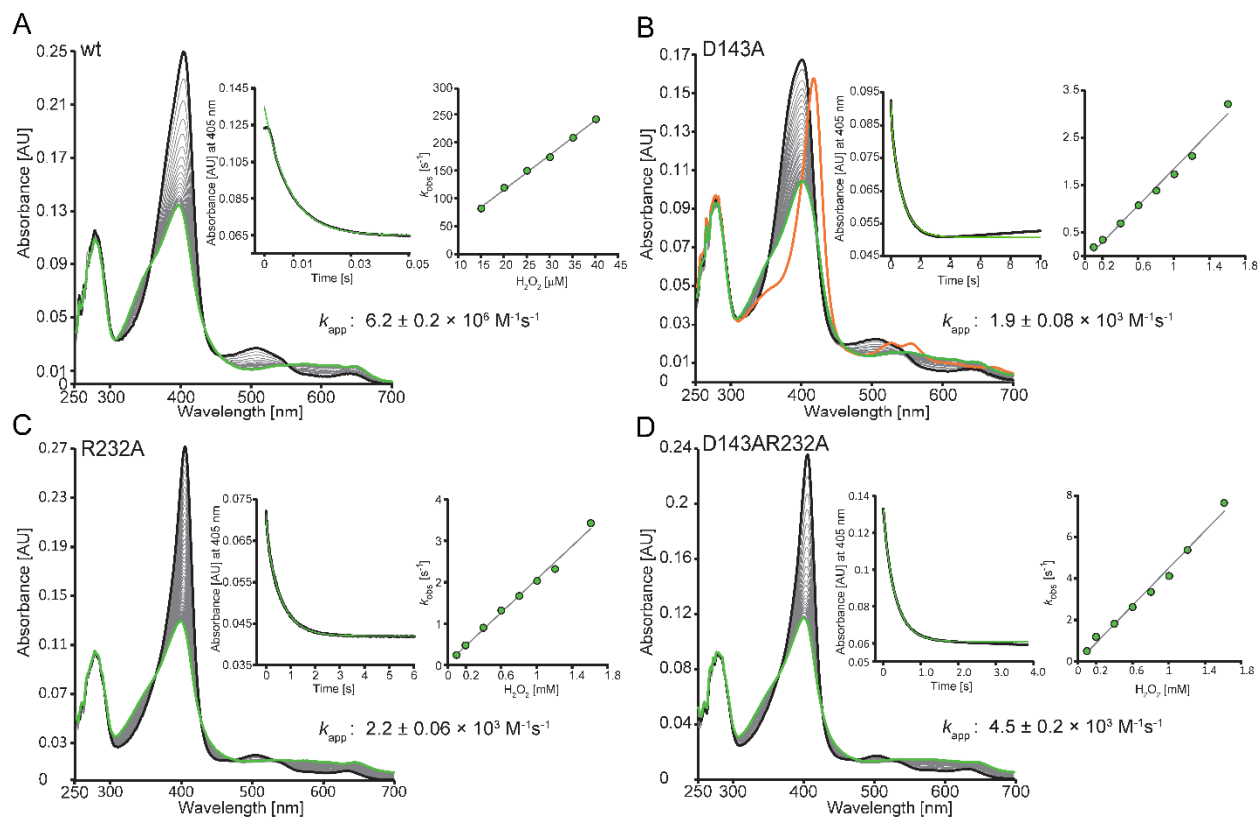


Figure 4. Kinetics of Compound I formation of wild-type *KpDyP* and the variants D143A, R232A and D143A/R232A at pH 7.0. Spectral transition upon the reaction of 2 μM wild-type (A), D143A (B), R232A (C) and D143A/R232A (D) with 20 μM (wild-type) or 800 μM (variants) hydrogen peroxide. Insets depict typical time traces at 405 nm (black) and the corresponding single- or double-exponential fits (green). Additionally, insets show the corresponding linear plots of k_{obs} versus hydrogen peroxide concentration.

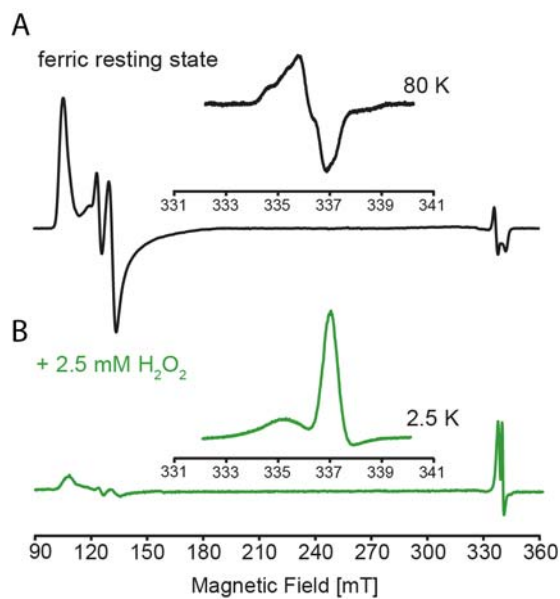


Figure 5. Low temperature CW EPR of wild-type *KpDyP* and Compound I. (A) X-band CW EPR spectrum of wild-type *KpDyP*. The inset shows the organic radical signature of the resting state at 80 K. (B) X-band CW-EPR spectrum of *KpDyP* Compound I formed by addition of a 5-fold stoichiometric excess of hydrogen peroxide. The inset shows the porphyrin radical signature observed at 2.5 K.

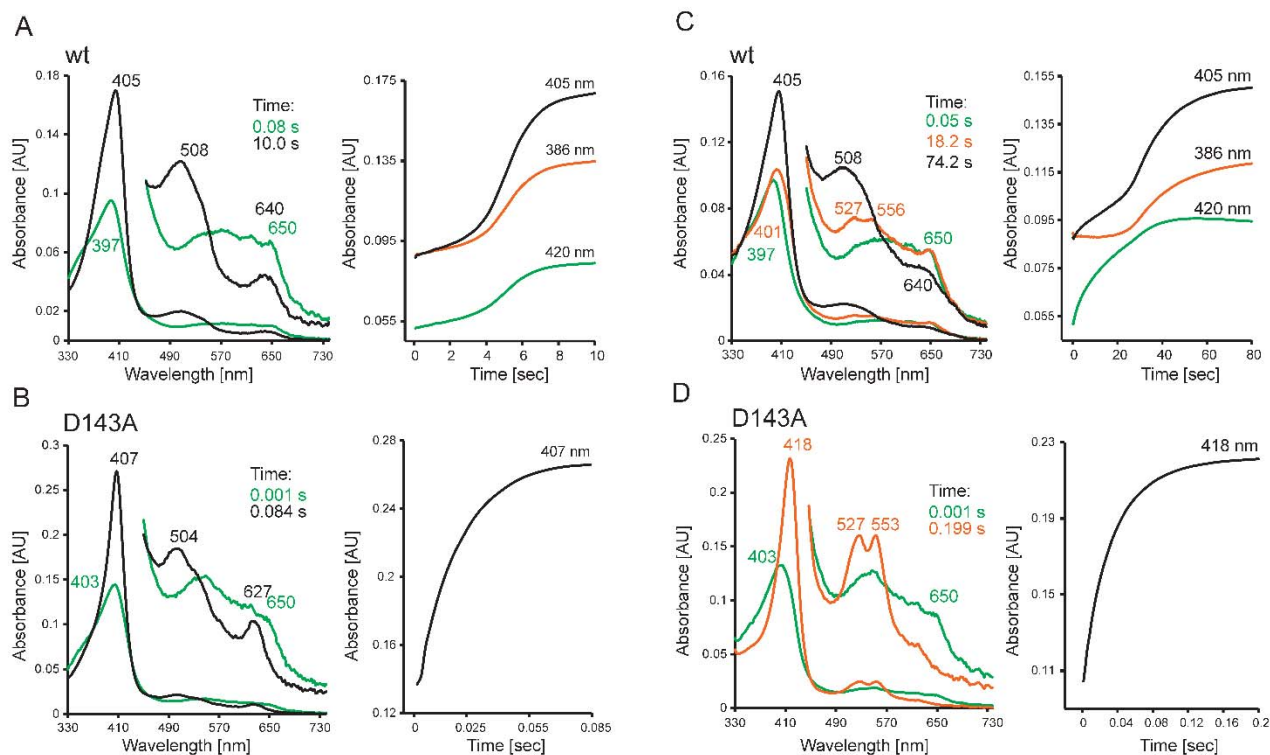


Figure 6. Reaction of wild-type *KpDyP* and D143A Compound I with thiocyanate and serotonin. (A, C) Reaction of wild-type Compound I with thiocyanate (A) and serotonin (C) at pH 7.0 followed by the sequential stopped-flow mode. Compound I (green spectrum) was preformed by mixing 2 μM ferric *KpDyP* with 4 μM H_2O_2 in 50 mM phosphate buffer, pH 7.0. After 100 ms delay time 1 mM thiocyanate (A) or 50 μM serotonin (C) were added. (B, D) Reaction of D143A Compound I with thiocyanate (B) and serotonin (D) at pH 7.0 followed by the sequential stopped-flow mode. Compound I (green spectrum) was preformed by mixing 2 μM ferric D143A with 1 mM μM H_2O_2 in 50 mM phosphate buffer, pH 7.0. After 3000 ms delay time 10 μM thiocyanate (A) or 1 mM serotonin (C) were added. Ferric spectra are shown in black, oxoiron(IV)-type Compound II spectra are shown in orange. Relevant absorption maxima and time points of selection of the spectra are depicted

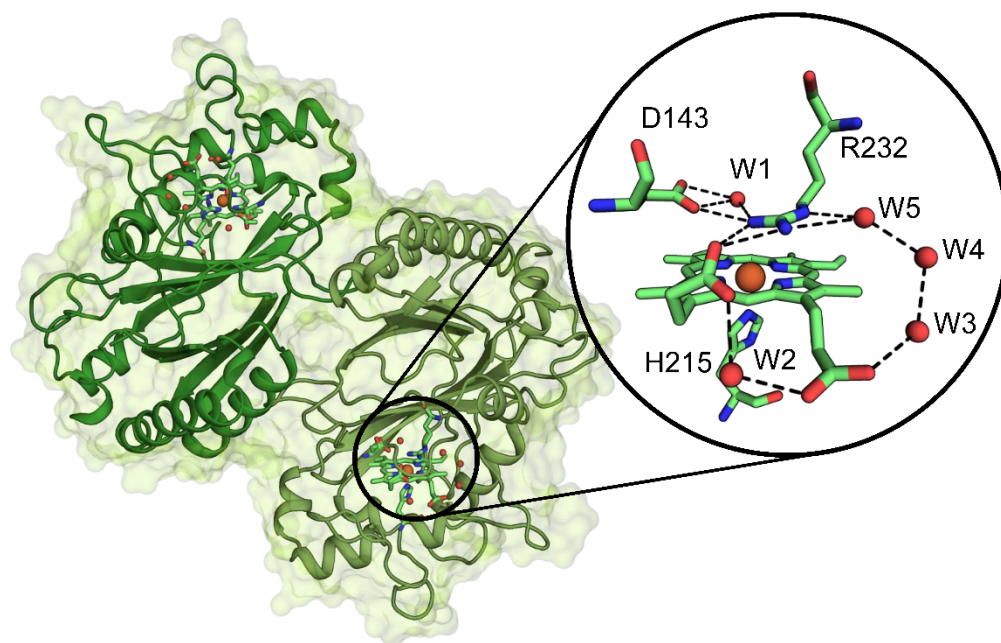


Figure 7. Overall and active site crystal structure of wild-type *KpDyP*. The dimeric structure of *KpDyP* is shown as cartoon (green). Heme prosthetic groups are depicted as sticks, the heme iron is shown as an orange sphere. The round inset shows a detailed view of the active site amino acid residues D143 and R232 (distal) and H215 (proximal) and the heme *b* moiety as a stick representation. Hydrogen bonding networks involving the distal residues and the heme *b* propionates are shown as dashed lines, water molecules (W) and heme iron are depicted as red and orange spheres, respectively.

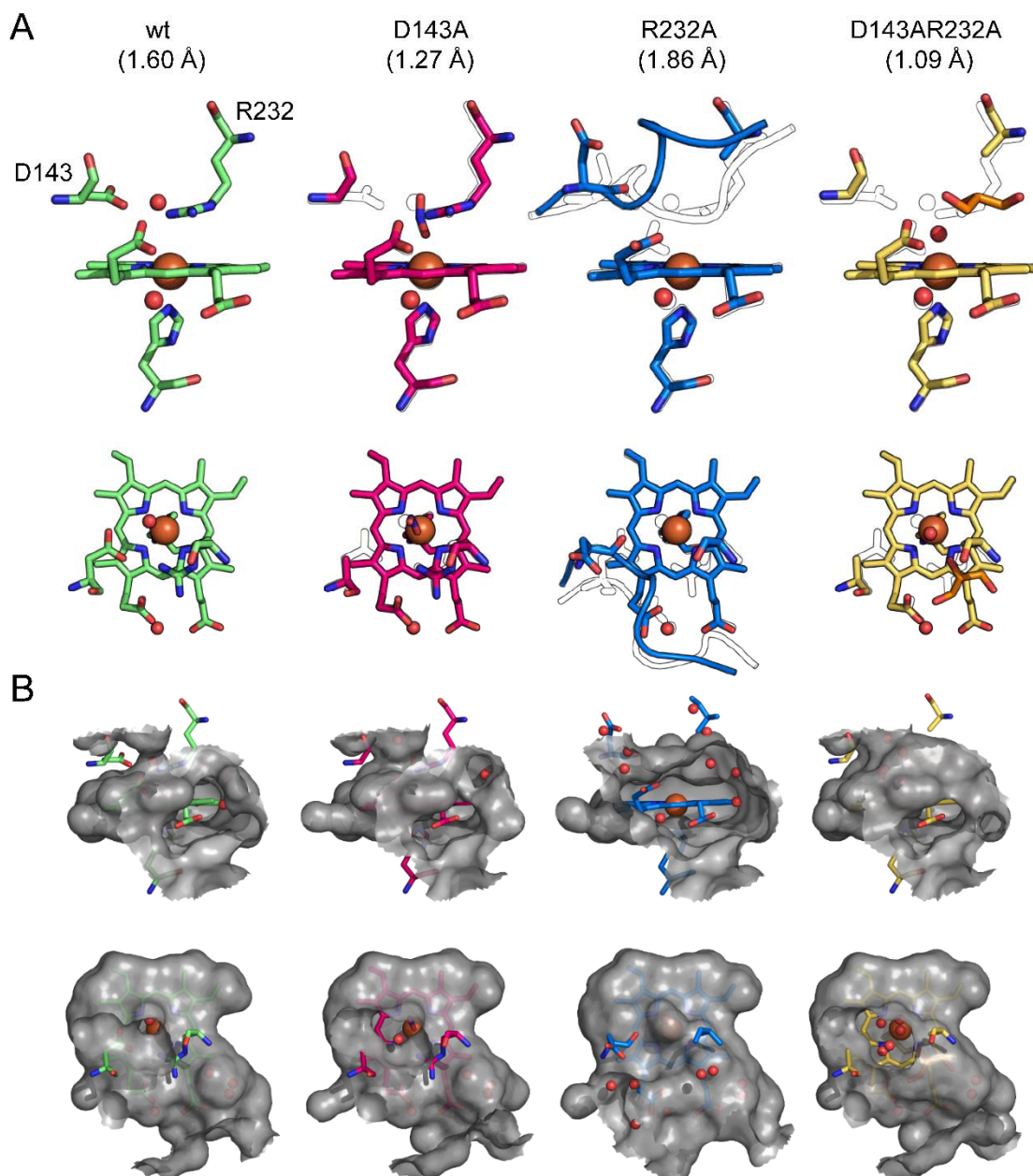


Figure 8. Comparison of the active site architecture of wild-type *KpDyp* and the variants D143A, R232A and D143A/R232A. (A) Representation of the active site residues D143, R232 and H215 and the heme *b* moiety shown from the front (first row) and top (second row). Relevant water molecules are shown as red spheres, nitrite (D143A structure) is shown in blue and glycerol (D132A/R232A structure) is shown in orange. In all mutants structure the wild-type structure is depicted as black outline for comparison. Additionally, the backbones of residues 141-148 is shown in the R232A structure together with the respective wild-type conformation (black outline). (B) Surface of the active site and access channels shown in a 6 Å radius from the heme iron colored in gray (semitransparent), shown from the front (first row) to visualize the surface accessible propionates and from the top (second row) to show the distal access channel

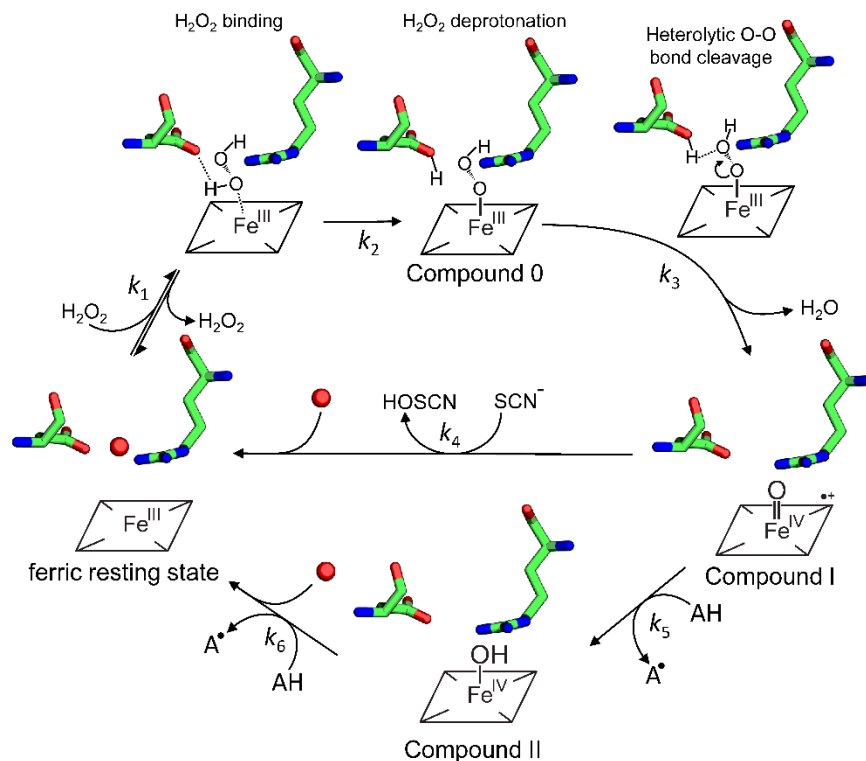


Figure 9. Proposed reaction mechanism for Compound 0, Compound I and Compound II formation in B-class DyPs. Hydrogen peroxide enters the narrow distal heme access channel, binds (k_1) and is deprotonated by D143 (Compound 0 formation). Heterolytic cleavage of the O-O bond (k_3) forms Compound I [oxoiron(IV) porphyrin radical] (k_3), which is reduced by either two-electron donors like thiocyanate (SCN⁻) directly to the ferric resting state thereby producing hypothiocyanite (HOSCN) (k_4) or by one-electron donors like serotonin (AH) to Compound II [oxoiron(IV) species] (k_5) thereby producing the corresponding radical (A[•]). Finally, a second one-electron donor (AH) reduces Compound II to the ferric resting state (k_6).

Table 1. EPR simulation parameters of spectra from wild-type and KpDyP variants (experimental error: ± 0.01 for the g values, ± 0.0005 for the E/D -ratio and $\pm 1\%$ for the contribution) compared to EPR data of other heme peroxidases. HRP, horseradish peroxidase; MtKatG, catalase-peroxidase from *Mycobacterium tuberculosis*; MaCld, chlorite dismutase from *Magnetospirillum* sp.; CCld, chlorite dismutase from the cyanobacterium *Cyanospora* sp. PCC7425; TcDyP, dye-decolorizing peroxidase from *Thermomonospora curvata*; AauDyP, dye-decolorizing peroxidase from *Auricularia auricula-judae*; NdCld, chlorite dismutase from *Nitrospira defluvii*; RjDyP, dye-decolorizing peroxidase from *Rhodococcus jostii* RHA1. TBD, to be determined; NR, not reported; † Readout values.

		g_x^{eff}	g_y^{eff}	g_z^{eff}	g_x	g_y	g_z	E/D	I (%)	Reference
KpDyP wt	HS1	6.44	5.12	1.98	1.93	1.93	2	0.0288	77.3	this work
	HS2	6.25	5.41	1.99	1.95	1.95	2	0.0178	22	
	Radical	-	-	-	TBD	TBD	TBD	-	0.7	
KpDyP R232A	HS1	6.06	5.69	1.99	1.96	1.96	2	0.0076	67.2	this work
	HS2	6.2	5.52	1.99	1.95	1.95	2	0.0148	23.9	
	HS3	6.05	5.88	2	1.99	1.99	2	0.0036	8.9	
KpDyP D143A	HS1	5.99	5.85	2	1.97	1.97	2	0.0029	40.7	this work
	HS2	6.13	5.69	1.94	1.97	1.97	2	0.0097	48.2	
	HS3	6.43	5.15	1.97	1.94	1.94	2	0.0279	11.1	
KpDyP D143A/R232A	HS1	6.13	5.61	1.99	1.96	1.96	2	0.0086	91.7	this work
	HS2	6.49	5.21	1.98	1.96	1.96	2	0.0220	8.3	
HRP	HS	6.35	5.65	2	NR	NR	NR	NR	100	(67)
MtKatG	HS1	5.86	5.86	2	NR	NR	NR	NR	NR	(68)
	HS2	6.03	5.55	2	NR	NR	NR	NR	NR	
	HS3	6.35	5.37	2	NR	NR	NR	NR	NR	
	HS4	6.49	5.1	2	NR	NR	NR	NR	NR	
MaCld	HS1	6.72	5.05	1.96	1.97	1.97	2	0.0380	6.5	(30)
	HS2	6.29	5.45	1.99	1.97	1.97	2	0.0177	93.5	
CCld	HS1	5.93	5.8	2	NR	NR	NR	0.002	62	(32)
	HS2	6.05	5.65	2	NR	NR	NR	0.008	28	
	LS	-	-	-	2.8	2.28	1.85	-	10	
TcDyP A-class†	HS	6.2	5.5	2	NR	NR	NR	NR	100	(23)
AauDyP A-class pH 3†	HS1	5.9	5.9	2	NR	NR	NR	NR	NR	(22)
	HS2	6.2	5.4	2	NR	NR	NR	NR	NR	
NdCld	HS1	5.50	6.17	1.99	NR	NR	NR	0.014	49	(69)
	HS2	5.95	5.95	1.99	NR	NR	NR	NR	19	
	LS1	-	-	-	2.98	2.25	1.88	-	15	
	LS2	-	-	-	3.15	2.25	1.80	-	16	
RjDyP A-class†	HS	6.32	5.45	1.97	NR	NR	NR	NR	NR	(6)
RjDyP B-class†	HS	6.09	5.45	1.99	NR	NR	NR	NR	NR	(6)

Table 2. Crystallization conditions, data collection, and refinement statistics for wild-type and KpDyP variants. Values in parentheses are for the highest resolution shell.

Data collection:	wild-type	D143A	R232A	D143A/R232A
Wavelength	0.97949	0.966	0.966	0.966
Resolution range	52.22 - 1.6 (1.657 - 1.6)	52.68 - 1.27 (1.315 - 1.27)	57.07 - 1.86 (1.927 - 1.86)	48.16 - 1.09 (1.129 - 1.09)
Space group	P 1 2 ₁ 1	P 1 2 ₁ 1	P 6 ₅ 2 2	P 1 2 ₁ 1
Unit cell	a = 50.52 b = 75.85 c = 75.64 α = 90 β = 107.86 γ = 90	a = 50.76 b = 76.69 c = 76.14 α = 90 β = 107.79 γ = 90	a = 91.16 b = 91.16 c = 247.82 α = 90 β = 90 γ = 120	a = 50.62 b = 76.31 c = 75.94 α = 90 β = 107.92 γ = 90
Total reflections	215756 (17146)	346778 (35130)	332227	641984 (58829)
Unique reflections	69426 (6619)	142004 (14135)	51833 (4908)	224631 (22440)
Multiplicity	3.1 (2.6)	2.4 (2.5)	6.4 (6.6)	2.9 (2.6)
Completeness (%)	96.86 (93.09)	97.21 (96.98)	99.26 (96.57)	98.45 (98.58)
Mean I/ σ (I)	F (2.21)	16.61 (2.63)	12.11 (1.32)	10.82 (1.28)
Wilson B-factor	17.73	12.78	27.25	11.17
Refinement:				
R-merge	0.04149 (0.4457)	0.03012 (0.4241)	0.1134 (1.701)	0.04589 (0.691)
R-meas	0.05004	0.03792	0.1235 (1.847)	0.05555
R-pim	0.02764	0.02269	0.04821	0.0309 (0.4891)
CC1/2	0.999 (0.802)	0.999 (0.794)	0.998 (0.674)	0.999 (0.574)
CC*	1 (0.944)	1 (0.941)	1 (0.897)	1 (0.854)
Reflections used in	69394 (6619)	141989 (14134)	51706 (4905)	224597 (22434)
Reflections used for R-free	3418 (335)	6954 (652)	2566 (247)	11225 (1135)
R-work	0.1281 (0.1757)	0.1147	0.1677	0.1246 (0.2533)
R-free	0.1668 (0.2198)	0.1406 (0.2212)	0.2074	0.1495 (0.2747)
CC(work)	0.973 (0.935)	0.977 (0.939)	0.969 (0.797)	0.978 (0.802)
CC(free)	0.966 (0.893)	0.973 (0.909)	0.950 (0.733)	0.972 (0.762)
Nr. of non-hydrogen atoms	5326	5682	5219	5817
macromolecules	4689	4781	4644	4928
ligands	112	106	87	112
solvent	525	795	488	777
Protein residues	596	602	598	602
RMS(bonds)	0.007	0.01	0.004	0.010
RMS(angles)	0.97	1.08	0.73	1.11
Ramachandran favored (%)	98.31	98.83	97.98	98.49
Ramachandran allowed (%)	1.69	1.17	1.85	1.51
Ramachandran outliers (%)	0	0	0.17	0
Rotamer outliers (%)	0.82	0.4	0.62	0.20
Clashscore	1.37	1.17	0.97	1.70
Average B-factor	21.26	18.06	33.5	16.61
macromolecules	19.93	15.81	32.81	14.51
ligands	18.2	12.18	31.83	12.01
solvent	33.75	32.34	40.35	30.61

Roles of distal aspartate and arginine of B-class dye-decolorizing peroxidase in heterolytic hydrogen peroxide cleavage

Vera Pfanzagl, Kevin Nys, Marzia Bellei, Hanna Michlits, Georg Mlynek, Gianantonio Battistuzzi, Kristina Djinovic-Carugo, Sabine Van Doorslaer, Paul G. Furtmüller, Stefan Hofbauer and Christian Obinger

J. Biol. Chem. published online August 2, 2018

Access the most updated version of this article at doi: [10.1074/jbc.RA118.004773](https://doi.org/10.1074/jbc.RA118.004773)

Alerts:

- [When this article is cited](#)
- [When a correction for this article is posted](#)

[Click here](#) to choose from all of JBC's e-mail alerts